View metadata, citation and similar papers at core.ac.uk
brought to you by CORE
provided by UNT Digital Library

SANDIA REPORT
SAND2004-6185
Unlimited Release
Printed December 2004

Nano-electromechanical Oscillators (NEMOs) for RF Technologies

J.P. Sullivan, T.A. Friedmann, D.A, Czaplewski, C.W. Dyck, J.R. Webster, A.J. Carton, D.W. Carr, B.E.N. Keeler, J.R. Wendt, D.R. Tallant, B.L. Boyce, X. Chen, and J.M. Gibson

Prepared by Sandia National Laboratories
Albuquerque, New Mexico 87185 and Livermore, California 94550

Sandia is a multiprogram laboratory operated by Sandia Corporation,

a Lockheed Martin Company, for the United States Department of Energy's
National Nuclear Security Administration under Contract DE-AC04-94AL85000.

Approved for public release; further dissemination unlimited.

Issued by Sandia National Laboratories, operated for the United States Department of Energy by Sandia Corporation.

NOTICE: This report was prepared as an account of work sponsored by an agency of the United States Government. Neither the United States Government, nor any agency thereof, nor any of their employees, nor any of their contractors, subcontractors, or their employees, make any warranty, express or implied, or assume any legal liability or responsibility for the accuracy, completeness, or usefulness of any information, apparatus, product, or process disclosed, or represent that its use would not infringe privately owned rights. Reference herein to any specific commercial product, process, or service by trade name, trademark, manufacturer, or otherwise, does not necessarily constitute or imply its endorsement, recommendation, or favoring by the United States Government, any agency thereof, or any of their contractors or subcontractors. The views and opinions expressed herein do not necessarily state or reflect those of the United States Government, any agency thereof, or any of their contractors.

Printed in the United States of America. This report has been reproduced directly from the best available copy.

Available to DOE and DOE contractors from
U.S. Department of Energy
Office of Scientific and Technical Information
P.O. Box 62
Oak Ridge, TN 37831

Telephone: (865)576-8401
Facsimile: (865)576-5728
E-Mail: reports@adonis.osti.gov
Online ordering: http://www.osti.gov/bridge

Available to the public from
U.S. Department of Commerce
National Technical Information Service
5285 Port Royal Rd
Springfield, VA 22161

Telephone: (800)553-6847
Facsimile: (703)605-6900
E-Mail: orders@ntis.fedworld.gov
Online order: http://www.ntis.gov/help/ordermethods.asp?loc=7-4-0#online

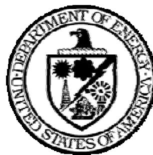

SAND2004-6185
Unlimited Release
Printed December 2004

Nano-electromechanical Oscillators (NEMOs) for RF Technologies

J. P. Sullivan, T. A. Friedmann, and D. A. Czaplewski
Nanostructure and Semiconductor Physics Department

C. W. Dyck, J. R. Webster, and A. J. Carton
RF Microsystems Technologies Department

D. W. Carr and B. E. N. Keeler
MEMS Device Technologies Department

J. R. Wendt
Photonic Microsystems Technology Department

D. R. Tallant
Materials Characterization Department

B. L. Boyce
Microsystem Materials and Mechanical Behavior Department

Sandia National Laboratories
P.O. Box 5800
Albuquerque, NM 87185

and

X. Chen[1,2] and J. M. Gibson[2]
[1]Cedarville Univ., Cedarville, OH 45314
[2]Argonne National Lab, Argonne, IL 60439

Abstract

Nano-electromechanical oscillators (NEMOs), capacitively-coupled radio frequency (RF) MEMS switches incorporating dissipative dielectrics, new processing technologies for tetrahedral amorphous carbon (ta-C) films, and scientific understanding of dissipation mechanisms in small mechanical structures were developed in this project. NEMOs are defined as mechanical oscillators with critical dimensions of 50 nm or less and resonance frequencies approaching 1 GHz. Target applications for these devices include simple, inexpensive clocks in electrical circuits, passive RF electrical filters, or platforms for sensor arrays. Ta-C NEMO

arrays were used to demonstrate a novel optomechanical structure that shows remarkable sensitivity to small displacements (better than 160 fm/Hz$^{1/2}$) and suitability as an extremely sensitive accelerometer. The RF MEMS capacitively-coupled switches used ta-C as a dissipative dielectric. The devices showed a unipolar switching response to a unipolar stimulus, indicating the absence of significant dielectric charging, which has historically been the major reliability issue with these switches. This technology is promising for the development of reliable, low-power RF switches. An excimer laser annealing process was developed that permits full in-plane stress relaxation in ta-C films in air under ambient conditions, permitting the application of stress-reduced ta-C films in areas where low thermal budget is required, e.g. MEMS integration with pre-existing CMOS electronics. Studies of mechanical dissipation in micro- and nano-scale ta-C mechanical oscillators at room temperature revealed that mechanical losses are limited by dissipation associated with mechanical relaxation in a broad spectrum of defects with activation energies for mechanical relaxation ranging from 0.35 eV to over 0.55 eV. This work has established a foundation for the creation of devices based on nanomechanical structures, and outstanding critical research areas that need to be addressed for the successful application of these technologies have been identified.

CONTENTS

1.0 Executive Summary 7
2.0 Introduction 9
2.1 References 9
3.0 Fluctuation Microscopy of ta-C 11
3.1 Introduction 11
3.2 Experiment and Results 11
3.3 References 14
4.0 Laser Annealing of ta-C 16
4.1 Introduction 16
4.2 Experimental Details 17
4.3 Results 19
4.4 Discussion 25
4.5 Conclusions 27
4.6 References 28
5.0 MEMS and NEMS Oscillators 30
5.1 Introduction 30
5.2 Theory 30
5.3 Oscillator Design 35
5.4 Device Fabrication 38
5.5 Measurement 39
5.6 Results and Discussion 41
5.7 Conclusions 47
5.8 References 47
6.0 NEMOs Optomechanical Structures 49
6.1 Introduction 49
6.2 Experiment and Results 49
6.3 Conclusion 53
6.4 References 53
7.0 RF MEMS Switches with ta-C Dielectrics 55
7.1 Introduction 55
7.2 Fabrication 55
7.3 Results and Discussion 56
7.4 Conclusion 58
7.5 References 58

8.0 Future 60
8.1 References 61
9.0 Acknowledgments 62

1.0 Executive Summary

This report describes research that was performed as part of a project to develop both new device technologies and scientific understanding in areas related to radio frequency (RF) microelectromechanical systems (MEMS). A number of advances in nanomechanical oscillator devices and improvements in RF MEMS switches were made during the course of the project. Many of these advances benefited from breakthroughs in the understanding of the properties and processing of a unique Sandia-developed MEMS material, teterahedral amorphous carbon (ta-C), which was the material of focus in this effort. Another important aspect of this work was the development of a research program aimed at understanding materials properties and mechanical performance in small structures, i.e. the field of nanomechanics.

The most significant nano-electromechanical oscillator (NEMO) devices developed in this project consisted of arrays of oscillators exhibiting a dominant in-plane transverse mode of vibration and critical dimensions as small as 50 nm (see Fig. 1.1). These structures were used for identifying intrinsic mechanical dissipation mechanisms in small oscillators of ta-C, and they formed the key component of a new, extremely sensitive optomechanical device for sensing small displacements (which is of especial importance in accelerometers). The most important development in the area of RF MEMS switches was the development of a capacitively-coupled RF switch technology that incorporates ta-C as a dissipative dielectric (see Fig. 1.2). This technology offers a solution for significantly improving RF switch lifetimes through the reduction or elimination of failure modes associated with dielectric charging or in-use stiction. In addition to these device developments, a breakthrough was made in the processing of ta-C for MEMS. A laser annealing technology was developed that may permit the processing of ta-C films with extremely low thermal budget, enabling, for example, the easy integration of ta-C MEMS or sensors with Si CMOS electronics. Lastly, the fundamental studies of internal dissipation in MEMS and NEMOs that were made in this project shed new insight into the mechanisms that limit mechanical dissipation in small structures, and this research has identified the important areas of nanomechanics research that need to be pursued to enable the widespread development of devices or sensors based on nanomechanical oscillators.

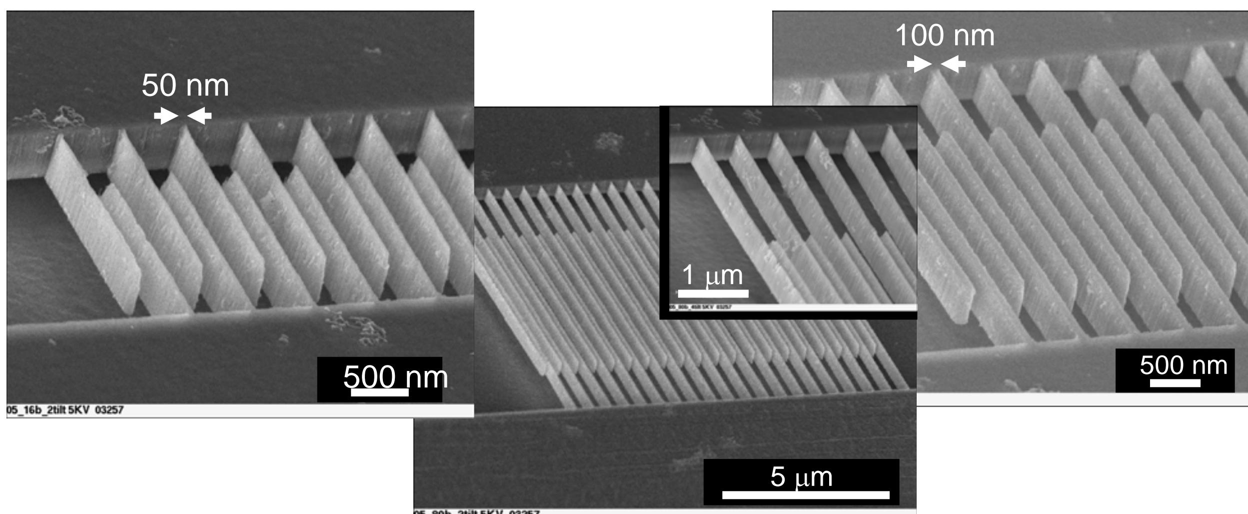

Fig. 1.1. Examples of tetrahedral amorphous carbon nano-electromechanical oscillators that were developed in this project.

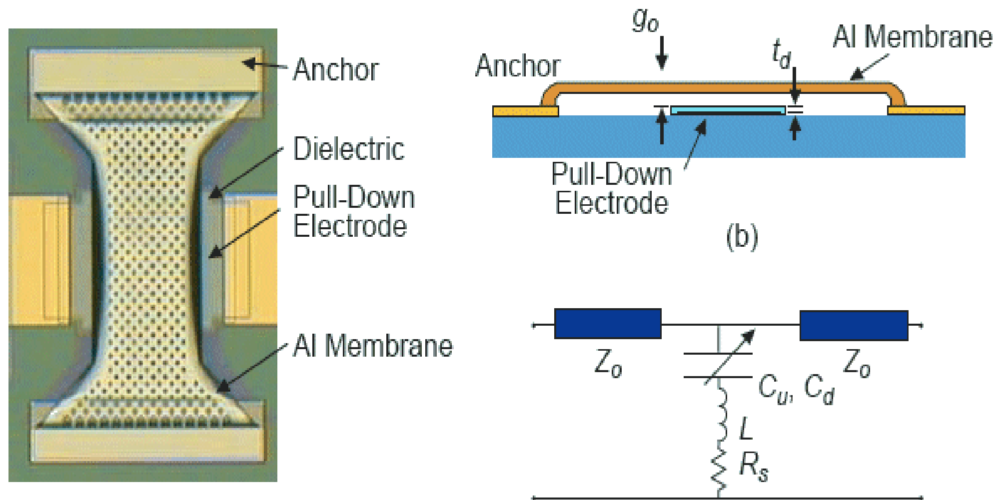

Fig. 1.2. An example of one of the RF MEMS switches incorporating a ta-C charge dissipating dielectric that was developed in this project. A top-view of the structure is shown on the left with a side view schematic and equivalent circuit on the right.

2.0 Introduction

The miniaturization of mechanical structures in the form of micro- or nano-electromechanical systems (MEMS or NEMS) offers promise for achieving small devices with new or significantly improved function. One area of especial interest is the development of radio frequency (RF) MEMS, which may be defined as MEMS that are integrated with RF electrical circuits. At least two different uses are envisioned for MEMS in RF technologies. The most ambitious, i.e. most challenging to achieve, technology is the creation of small mechanical oscillators with critical dimensions down to the 10's of nm length scale, which we call nano-electromechanical oscillators (NEMOs). Due to their small size, these structures have natural mechanical resonant frequencies that can approach 1 GHz. They can be integrated into RF electrical circuits for use as narrow bandpass filters of electrical signals [1]. However, achieving small mechanical oscillators with high resonant frequency and high quality factor, Q, can be a very challenging proposition. A more mature RF MEMS technology is RF MEMS switches. These structures are used to switch RF circuits on or off, permitting, for example, a tunable antennae array, etc. Here, the challenge is to achieve a reliable switch – one that can turn on and off reliably for millions of cycles [2].

In this project, two RF MEMS technologies were developed: (1) NEMOs for high frequency filters and (2) capacitively-coupled RF MEMS switches incorporating dissipative dielectrics. One of the novel approaches employed here is to create the NEMOs and dissipative dielectrics from a unique form of carbon known as tetrahedral amorphous carbon (ta-C) or, alternatively, amorphous diamond (a-D or aD). The stress-free form of this material was invented at Sandia, and it has been used in the past for conventional MEMS [3,4]. The material has properties that make it particularly suitable for these applications, including an extremely high elastic modulus (enables high frequencies), an intrinsically hydrophobic surface (reduces release or in-use stiction), a very smooth surface (enables thin dielectrics with controlled thickness), and a tunable electrical conductivity (enables charge dissipation) [5].

The approach taken in this project required concerted activities in fundamental materials science (understanding the properties of ta-C for its use in NEMOs and RF MEMS switches), developing and assessing MEMS and NEMS oscillators, developing the applications of NEMS oscillators, and creating and assessing RF MEMS switches that contain ta-C dielectrics. This Report is structured along the same lines: in the first chapters we describe a new characterization of the structure and temperature-induced structural relaxation of ta-C [6], including the development of a laser annealing stress relaxation technology [7]; then the creation and measurement of ta-C MEMS and NEMS oscillators are discussed with a particular emphasis on understanding the mechanisms of mechanical dissipation in this material [8]; this is followed by a discussion of a novel optomechanical structure that employs an array of NEMOs as its key functional component [9,10]; lastly, we discuss the creation and analysis of RF MEMS switches employing a dissipative dielectric [11,12].

2.1 References

1. see, for example, C. T.-C. Nguyen, L. P. B. Katechi, and G. M. Rebeiz, Proc. IEEE **86**, 1756 (1998).
2. C. Goldsmith, et al., IEEE MTT-S Int. Microw. Symp. Dig. **1**, 227 (2001).

3. T. A. Friedmann and J. P. Sullivan, "Method of Forming a Stress Relieved Amorphous Tetrahedrally-Coordinated Carbon Film," U.S. Patent no. 6,103,305 (2000).
4. J. P. Sullivan, T. A. Friedmann, C. I. Ashby, M. P. de Boer, W. K. Schubert, R. J. Shul, R. J. Hohlfelder, and D. A. LaVan, "Amorphous Diamond MEMS and Sensors", SAND Report SAND2002-1755 (2002).
5. J. P. Sullivan, T. A. Friedmann, M. P. de Boer, D. A. LaVan, R. J. Hohlfelder, C. I. H. Ashby, M. T. Dugger, M. Mitchell, R. G. Dunn, and A. J. Magerkurth, Proc. Materials Research Society Symposium **657**, EE711 (2001).
6. X. Chen. J. P. Sullivan, T. A. Friedmann, and J. M. Gibson, Appl. Phys. Lett. **84**, 2823 (2004).
7. T. A. Friedmann, J. P. Sullivan, D. R. Tallant, and B. L. Boyce, submitted to J. Appl. Phys. (2004).
8. D. A. Czaplewski, J. P. Sullivan, T. A. Friedmann, J. R. Wendt, D. W. Carr, and B. E. N. Keeler, accepted for publication in J. Appl. Phys. (2004).
9. D. W. Carr, J. P. Sullivan, and T. A. Friedmann, Optics Lett. **28**, 1636 (2003).
10. B. E. N. Keeler, D. W. Carr, J. P. Sullivan, T. A. Friedmann, and J. R. Wendt, Optics Lett. **29**, 1182 (2004).
11. J. R. Webster, C. W. Dyck, T. A. Friedmann, J. P. Sullivan, C. D. Nordquist, A. J. Carton, G. M. Kraus, and G. D. Schmidt, Proc. of the SPIE **5344**, 71 (2004).
12. J. R. Webster, C. W. Dyck, J. P. Sullivan, T. A. Friedmann, and A. J. Carton, Electron. Lett. **40**, 43 (2004).

3.0 Fluctuation Microscopy of ta-C

3.1 Introduction

Hydrogen-free amorphous diamond-like carbon (ta-C) films have stimulated great interest because of their useful properties, such as high hardness, chemical inertness, thermal stability, wide optical gap, and negative electron affinity [1]. Consequently, they may have various potential applications in mechanical and optical coatings, MEMS systems, chemical sensors and electronic devices [2]. Amorphous diamond-like carbon films often contain a significant amount of four-fold or sp^3 bonded carbon, in contrast to amorphous carbon films prepared by evaporation or sputtering which consist mostly of three-fold or sp^2 bonded carbon [3]. Structural configurations of these three-fold and four-fold carbon atoms determine the properties of these amorphous diamond-carbon films. Although the ratio of three-fold and four-fold carbon has been studied with Raman spectroscopy [4], electron-energy-loss spectroscopy (EELS) [5], and nuclear magnetic resonance [6] there is a lack of knowledge regarding key questions such as the spatial distribution of the three-fold and the four-fold carbon atoms in the film, and what local structures those three-fold and four-fold carbon atoms take. Conventional diffraction techniques only yield the radial distribution function (RDF) which is essentially a two-body correlation function describing short-range order. The above structural issues however involve atomic arrangements beyond short-range order.

Fluctuation microscopy utilizes a phenomenon called speckle patterns [7]. Speckle patterns are generated by interference under coherent scattering conditions. In a transmission electron microscope (TEM) dark field image, the intensity of each pixel is only contributed by electrons scattered by a small cylindrical column of atoms [8], whose radius is defined by the resolution and whose height is the sample thickness. Therefore, the intensity fluctuation is directly related to the local structure change in each small volume of the sample. To the first order approximation [9], the intensity fluctuation across the whole image is given by:

$$\left\langle I^2(\vec{k})\right\rangle - \left\langle I(\vec{k})\right\rangle^2 \propto \left\langle \sum_{i\neq j, l\neq m} \exp[i\vec{k}\bullet(\vec{r}_{ij}-\vec{r}_{lm})]\right\rangle - \left\langle \sum_{i\neq j}\exp[i\vec{k}\bullet\vec{r}_{ij}]\right\rangle \left\langle \sum_{l\neq m}\exp[i\vec{k}\bullet\vec{r}_{lm}]\right\rangle \qquad (3.1)$$

where k is the momentum transfer value at which the dark-field image is taken.

Equation 3.1 shows that the intensity fluctuation involves two pairs of atoms. By measuring the intensity fluctuation in TEM dark-field images as a function of the momentum transfer value k, atomic correlation involving two pairs of atoms can be extracted. Any local structure correlation beyond a length scale defined by the resolution may be detected. This technique allows experimental access to medium-range order structures of amorphous materials that were inaccessible before. In this section, we report our fluctuation microscopy studies of amorphous diamond-like carbon films.

3.2 Experiment and Results

Amorphous diamond-like carbon films were fabricated by pulsed-laser deposition using a KrF laser (248 nm) and a graphite target. The deposition was performed at room temperature on to a polished Si(100) wafer up to a final thickness of 30 nm. The films are hydrogen free and

contain about 80% four-fold (sp^3) carbon with the rest being three-fold (sp^2) carbon. In this paper, we will present results from as-grown samples (no annealing after the growth) and samples that were annealed after growth at two different temperatures. The annealing condition consisted of heating in vacuum at $< 1 \times 10^{-5}$ Torr for a period of 30 min. at 600°C or 1000°C. Prior electrical and mechanical measurement have shown great differences in properties following post-deposition annealing in this temperature range [10].

Plan-view TEM samples were made from the films by core-drilling and chemical etching in HNO_3:HF:CH_3COOH (5:3:3). The film thickness under TEM observations is about 30 nm. Electron diffraction patterns were taken for each sample. The maximum k was 22.4 $Å^{-1}$.

To understand the short-range order in those films, we first measured the reduced radial distribution function from diffraction patterns. Small angle scattering was also cut off before the Fourier transform was performed in order to remove the strong electron dynamical effect. This cut-off should not affect our results because small angle scattering does not contribute to the term that yields the radial distribution function [11]. An edge smooth function was applied when the Fourier transform was performed. This procedure reduces artificial oscillations in the resultant radial distribution function. The RDF is an ensemble average of the short-range order structures (2 – 5 Å) of the whole sample[11].It cannot provide information on local structure changes at length scales larger than 5 Å, i.e., the medium-range order structures.

All experiments were conducted on a JEOL-4000EX microscope that had been set up for automated fluctuation microscopy data collection at the Electron Microscopy Center at Argonne National Lab. During an experiment, a series of dark-field images were taken on an area of the sample as a function of the tilting angle of the electron beam through reciprocal space. The same process is typically repeated for several different areas to gain good statistics. Normally a few hundred images are taken in a single experiment. The images were then processed by a script, removing distortions and applying Wiener filtering. The intensity fluctuation was eventually obtained as a function of the momentum transfer value. This variance function of k is directly related to a pair-pair correlation function that defines medium-range order at the nanometer scale.

Results of radial distribution functions are presented in figure 3.1. The average bond length is 1.52Å and the average bond angle is 72.6°. Up to 600°C, there are no pronounced differences between radial distribution functions for the un-annealed and annealed samples (after 1000°C annealing, there are significant differences that are due to graphitization, discussed below). Fig. 3.1 shows that short-range order information characterized by the RDF is not able to give account to property changes that occur in the diamond-like carbon films at the lower anneal temperatures.

Fluctuation microcopy results, however, reveal a clearer picture. Our results are presented in figure 3.2. The variance peaks at 4.9 nm^{-1} and 8.5 nm^{-1} are signatures of medium-range order or clustering on a length scale of about 1 nm, which is approximately the electron coherence length used in these measurements. The peak height is a function of the annealing temperature. When annealing was done at 1000°C, an additional peak shows up at 2.9 nm^{-1}, indicating a new ordered structure not present in the lower temperature films. Each peak corresponds to a type of local structure or ordering, represented by a narrow range of k values. The width of the peak, which is defined by the two minima of the peak, is proportional to the size of this structure unit, i.e. a large well-ordered structure would be represented by a narrow peak. Therefore the fact that the width of the peaks is not changing indicates that the *size* of the local structure units is not changing. The height of a peak is proportional to the *number* of the corresponding structure units

in the sample. Therefore, the variance vs. k plot indicates that the number of structural units, i.e. clusters, is increasing as the sample is annealed up to 600°C.

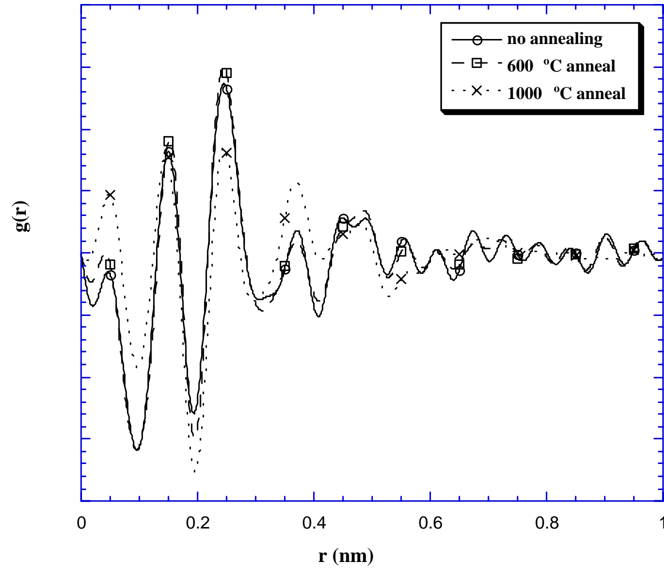

Fig. 3.1. Measured reduced distribution functions for a film without annealing and films annealed at 600°C and 1000°C. For films annealed up to 600°C, the short range order is similar.

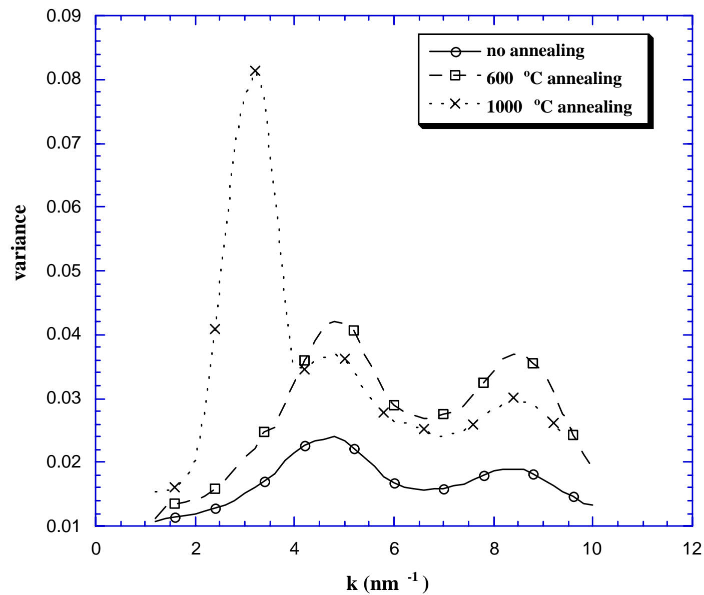

Fig. 3.2. Plots of the variance as a function of k for amorphous diamond-like carbon films with or without annealing. The medium range order, indicated by the peaks, is increased after thermal annealing. New structural ordering shows up in the 1000°C annealed film.

From solid state nuclear magnetic resonance measurements performed on amorphous diamond-like carbon films prepared in the same fashion as the films described here, it is known that both sp^3 and sp^2 chemical bonds are present in the material [12]. About 80% of the bonds are sp^3 (4-fold coordinated carbon) from the as-deposited condition through annealing temperatures up to 600°C [12]. At temperatures higher than 900°C, the majority of the bonds are sp^2 [12]. The peak positions in figure 3.2 for the as-deposited and 600°C annealed films are in approximate agreement with broad peaks, not shown, that were obtained from the calculated diffraction from a theoretical 64-atom cell of amorphous diamond-like carbon [13]. These peak positions are related to local structures adopted in the amorphous network and are dominated by the majority-phase diamond-like component in the material.

After 1000°C annealing, a new sharp peak forms. This peak is in good agreement with the (002) reflection of graphite, which arises from the interplanar spacing of graphite sheets. It is well-known that high temperature annealing leads to graphitization in diamond-like carbon films [12,14-16]. This is characterized by an increase in 3-fold to 4-fold carbon ratio determined by solid state NMR, EELS, near edge x-ray absorption fine structure, or the appearance of a Raman signature that is characteristic of glassy carbon (a disordered carbon material consisting of nearly 100% 3-fold coordinated carbon). Therefore, we identify the peak at 2.9 nm^{-1} with the presence of disordered graphite sheets in the film, similar to what is observed in glassy carbon. Importantly, the absence of this peak in the lower temperature films is a direct indication that graphite-like ordering is not present in as-deposited or low temperature amorphous diamond-like films.

The experimental results lead to several conclusions: (1) low temperature annealing (up to 600°C) produces measurable changes in structure in the amorphous diamond-like carbon films, (2) the dominant effect of annealing at 600°C is to increase the concentration of locally ordered structure units that have local diamond-like ordering, (3) these units are heterogeneously distributed through the sample at a length scale comparable to or greater than 1 nm, (4) 600°C annealing does not tend to increase the size of these structure units (the peaks do not become narrow), (5) annealing at 1000°C introduces distinct structural changes with the most pronounced being the presence of sheet-like, (002)-like, graphitic ordering in the sample with relatively large domains (a narrow peak), but this graphitic ordering is not present at lower temperatures. The change in local ordering that is apparent in amorphous diamond-like carbon following low temperature annealing has also recently been reported in a solid state NMR study [6]. Interestingly, the existence of heterogeneous ordering (or clustering) in amorphous diamond-like carbon films was also reported in a transmission electron microscopy study [17]. Taken together, these studies suggest that pronounced structural rearrangements may occur in amorphous diamond-like carbon films at modest temperatures, i.e. with low activation energies, while still retaining an amorphous structure that looks nearly identical by RDF analysis (figure 3.1). This finding suggests why stress relaxation may be unexpectedly facile in this system [10].

3.3 References

1. J. Robertson, Prog. Solid State Chem. **21**, 199 (1991).
2. J. P. Sullivan, T. A. Friedmann, K. J. Hjort, MRS Bull. **26**, 309 (2001).
3. J. Robertson, Adv. Phys. **35**, 317 (1986).

4. A. C. Ferrari, B. Kleinsorge, G. Adamopoulos, J. Robertson, W. I. Milne, V. Stolojan, L. M. Brown, A. LiBassi, and B. K. Tanner, J. Non-Cryst. Sol. **266-269**, 765 (2000).
5. P. J. Fallon, V. S. Veerasamy, C. A. Davis, J. Robertson, G. A. J. Amaratunga, W. I. Milne, and J. Koskinen, Phys. Rev. B **48**, 4777 (1993).
6. T. M. Alam, T. A. Friedmann, P. A. Schultz, and D. Sebastiani, Phys. Rev. B **67**, 245309 (2003).
7. J. M. Gibson and M.M. J. Treacy, Phys. Rev. Lett. **78**, 1074 (1997).
8. P. B Hirsh, A. Howie, R. B. Nicholson, and D. W. Pawshley, *Electron Microscopy of Thin Crystals*, (Butterworths, Washington, 1965).
9. X. Chen, J. M. Gibson, J. Sullivan and T. Friedmann, “Medium-range order structures of amorphous diamond-like carbon films”, Symposium W, Materials Research Society Spring meeting, April 16 –20, 2001.
10. J. P. Sullivan, T. A. Friedmann, and A. G. Baca, J. Electron. Mater. **26**, 1021 (1997).
11. S. R. Elliot, *Physics of Amorphous Materials*, (Longman Scientific & Technical, 1990).
12. T. M. Alam, T. A. Friedmann, and A. J. G. Jurewicz, in *Thin Films: Preparation, Characterization, Applications*, edited by Soriaga *et al.* (Kluwer Academic/Plenum, 2002), pp. 277-289.
13. P. A. Schultz and E. B. Stechel, Phys. Rev. B **57**, 3295 (1998).
14. T. A. Friedmann, K. F. McCarty, J. C. Barbour, M. P. Siegal, and D. C. Dibble, Appl. Phys. Lett. **68**, 1643 (1996).
15. S. Anders, J. Díaz, J. W. Ager, R. Y. Lo, and D. B. Bogy, Appl. Phys. Lett. **71**, 3367 (1997).
16. A. C. Ferrari, B. Kleinsorge, N. A. Morrison, A. Hart, V. Stolojan, and J. Robertson, J. Appl. Phys. **85**, 7191 (1999).
17. M. P. Siegal, D. R. Tallant, P. N. Provencio, D. L. Overmyer, R. L. Simpson, and L. J. Martinez-Miranda, Appl. Phys. Lett. **76**, 3052 (2000).

4.0 Laser Annealing of ta-C

4.1 Introduction

Hydrogen free tetrahedral amorphous-carbon (ta-C) thin films have a number of desirable properties for MEMS [1]. Compared to Si, ta-C thin films have higher hardness, stiffness, and wear resistance, lower friction coefficients, and are more resistant to chemical attack. In addition, ta-C surfaces are nearly hydrophobic reducing problems with adhesion upon release. Single level MEMS devices have been fabricated using complementary metal oxide semiconductor (CMOS) compatible techniques and these devices have been used to measure mechanical properties such as stress, stress gradients, fracture strength and fracture toughness [2-5]. Recently, we have fabricated radio-frequency capacitive switches with ta-C as the dielectric layer [6,7] and in-plane nanomechanical resonators combined with a novel optical measurement technique that have demonstrated ~0.1 pm/$\sqrt{\mathrm{Hz}}$ motion sensitivity [8,9].

In order to fabricate MEMS devices, it is necessary to control stress (< 10 MPa) and stress gradients (or radius of curvature < 1 m) to reduce problems with distortion and out-of-plane bending of released parts. This is a severe problem for ta-C since as-deposited films typically have 2-10 GPa of intrinsic stress. We use thermal annealing to reduce the growth stresses to manageable levels (<10 MPa) [10]. Typically, annealing temperatures of 650°C for several minutes are required to achieve full stress relief, and several deposition and annealing steps are required to grow ~1 μm thick films to avoid adhesion failures. We have shown that the stress relief kinetics in ta-C are similar to those deduced from a first-order chemical process, implying that the mechanism for stress relaxation is one of strain-relieving bond transformations that are activated with temperature [11]. We have also shown in a ^{13}C magic-angle-spinning nuclear-magnetic-resonance investigation [12] that there is a significant ordering that occurs upon annealing near 650°C, even though the structure remains amorphous with no measurable change in the 4-fold content. Higher temperature (~1100°C) longer time (~30 min.) anneals can lead to reduction of the 4-fold content with resultant degradation of the diamond-like properties [13,14].

It would be highly desirable to reduce the thermal budget for stress relief since this could enable the production of ta-C MEMS on top of CMOS circuits. One option is to reduce the annealing temperature and increase the annealing time, but this quickly becomes impractical since the required time increases exponentially with decreasing temperature [11]. Another possibility is to anneal at much higher temperatures for very short periods of time. This can be done easily using short pulse laser annealing to induce high surface temperatures without significantly disturbing the underlying substrate.

There have been many studies in the past on laser annealing of carbon films and potential applications [15-25]. Several authors have reported graphitization of DLC films and used this to write conducting lines [16], remove hydrogen [20], and create patterned structures. Others have worked above the ablation threshold to produce patterned structures [17,22-24]. There have been several reports of amorphous-to-crystalline phase transformations in laser-annealed carbon [26] and hydrogenated DLC [15,18,25] thin films. Nistor et al. [15] in a combined Raman and TEM study reported that small (2-7 nm) diamond crystals were formed under KrF excimer laser annealing; and that these films also showed increased ordering of the remaining amorphous graphitic phase. Weissmantel et al. [25] reported the formation of nanocrystalline diamond in amorphous carbon films grown by ion-beam assisted deposition while simultaneously irradiating

the growing film surface with an excimer laser beam. Majni et al. [26] laser annealed sputtered graphite films on Si using a XeCl excimer laser and reported the formation of both nanocrystalline SiC and diamond phases. They attributed SiC formation to the melting of the Si substrate by the laser pulse allowing rapid diffusion and phase transformation. None of these studies report on the effect of laser annealing on stress and there is no work that we are aware of on laser annealing of ta-C thin films.

In this section, we report on a systematic study of residual stress, bonding, and hardness of ta-C thin films on Si (100) substrates following excimer laser annealing. To understand the results of the experimental study, we performed finite element modeling (FEM) of the time and temperature dependence of the laser induced temperature response. We found that it was possible to completely relieve the *average* in-plane stress in ta-C thin films without significantly altering the bonding - similar to results found earlier on furnace annealed films [10]. However, significant stress gradients in the films were found due to large temperature gradients induced by the laser heating process.

4.2 Experimental Details

The ta-C thin films were prepared by pulsed laser deposition (PLD) using an excimer laser (248 nm, Lambda Physik LPX 315i), configured with unstable resonator optics, at high fluence (~100 J/cm^2) to ablate a pyrolytic graphite target in a vacuum chamber ($< 1 \times 10^{-6}$ Torr) onto 2.5 x 10 mm^2 pieces cleaved from a 25 mm diameter 250 μm thick Si (100) wafer. For this study films of 500, 1100, 1500, and 2000Å were grown. Film thicknesses were measured with a stylus profilometer (Tencor P-10).

The laser annealing was performed in air using a separate excimer laser (248 nm, Lambda Physik LPX 305) at 0.3 Hz repetition rate configured with stable resonator optics producing a 28 nsec pulse width. The output laser beam was passed through a homogenizer (Microlas) consisting of a 7 x 8 lenslet array that separates the beam into 56 separate beamlets that are imaged to a spot 2.7 x 46 mm^2 providing ±5% energy uniformity across the beam profile. The beam intensity was measured using a pyrolytic joule meter (Gentec ED-500), and was adjusted with an optical attenuator from 0 – 300 J/cm^2.

The stress in the ta-C films was measured using a laser-based wafer curvature technique (k-space associates) with laser spot spacings (corresponding to wafer curvature) recorded using a CCD detector. The wafer curvature was measured before and after deposition and during laser annealing. The experimental setup (Fig. 4.1) allowed for the simultaneous measurement of stress during the laser annealing process such that the change in stress for each laser pulse was recorded. The wafer curvature measurements were converted to stress using Stoney's equation [27].

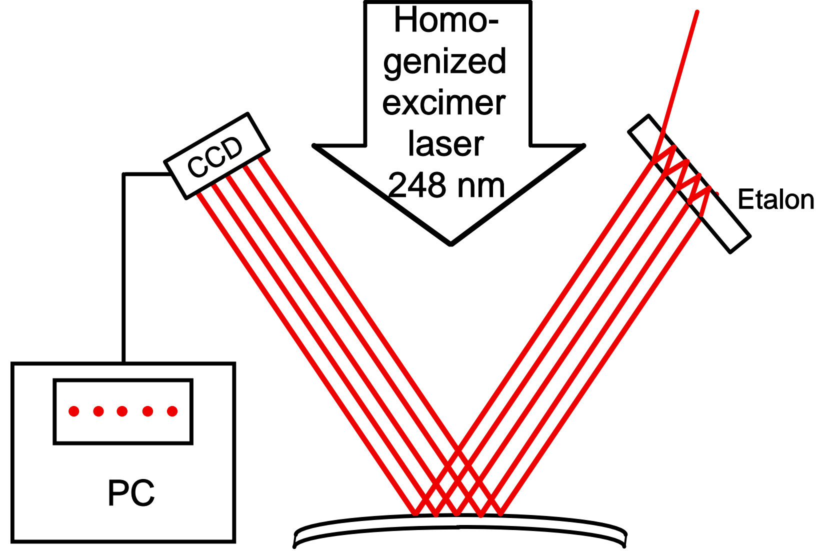

Fig. 4.1 Schematic of the experimental setup for laser annealing and stress measurement.

Raman measurements were made using the 514.5 nm line of an Argon ion laser at a power of 50 mW. Hardness measurements were made on the 1100Å thick films with a nanoindentor (Hysitron Triboscope) equipped with a Berkovich diamond tip. Each sample was indented 24 times to a load of 1060 μN (contact depth ~150Å) and the results averaged to give the final hardness value. The tip calibration was checked before and after the runs to ensure no significant changes occurred in the tip shape. Under these conditions, uncertainties in the tip calibration, deformation of the diamond tip, and the effects of a hard film on a relatively soft substrate can lead to significant errors in the absolute hardness numbers [28]. No attempt was made to correct the data for these potential errors implying the absolute magnitude of the hardness numbers could be significantly different from the reported numbers; however, these errors should be the same for all samples indented, and thus trends in the data are significant.

In order to gain insight into the experimental stress measurements, a series of calculations were carried out to estimate the time and temperature profile of the heat pulse generated by the laser annealing. The heat flow was assumed to be one-dimensional in nature with the laser light being converted instantaneously into heat upon absorption in the ta-C thin film. The one-dimensional heat equation with a source term becomes:

$$\frac{\partial T}{\partial t} = \frac{\alpha}{\rho C_p} I(z,t) + \frac{1}{\rho C_p} \frac{\partial}{\partial z}\left(\kappa \frac{\partial T}{\partial z}\right), \qquad (4.1)$$

where I(z,t) is the power density of the laser light at depth z and time t. T is the temperature and ρ, C_p, κ, and α are the density, specific heat, thermal conductivity and absorption coefficient respectively. Equation 4.1 was solved using a finite element approach described elsewhere [29]. The modeling included both the ta-C film and the silicon substrate. The temperature dependent thermal properties of silicon are well known and were taken from handbook values, but those for ta-C are not. The absolute accuracy of the calculations is limited due to this uncertainty. The ta-C density $\rho = 3.1$ g/cm^3, was taken from x-ray reflectivity measurements [30]. The ta-C absorption coefficient at 5 eV was estimated to be $\alpha = 10^6$, extrapolated from photothermal deflection spectroscopy absorption measurements on ta-C membrane samples [31], and assumed to be constant with temperature. The thermal conductivity was also assumed to be temperature independent at a room temperature value $\kappa = 0.03$ W/cmK [32]. We are unaware of any specific

heat data on ta-C thin films; therefore, the temperature dependent specific heat was assumed to be 80% that of diamond plus 20% of graphite using a parameterization developed by Fried et al. [33] The laser pulse was modeled in time as a square wave normalized to the experimentally measured energy density. The calculations were carried out on a personal computer using layer slices of 2 nm thickness and a time step of 1 ps out to 200 ns in time for all four sample thicknesses experimentally annealed. No attempt was made to include melting of Si in the model, as it was found that the Si substrate did not reach its melting point at 1410°C under most of the modeled experimental conditions.

4.3 Results

Fluence dependence at a given thickness

Fig. 4.2 depicts the normalized change in stress with increasing laser shots for samples of 1100Å thickness annealed at increasing laser fluence from 40 – 280 mJ/cm^2. (The initial stress for these samples was 7.1± 0.3 GPa.) Each curve is generated from a fresh sample and all of the samples were grown in the same deposition run. For all fluences below 250 mJ/cm^2 the stress decreases monotonically with increasing number of laser shots and the rate of decrease slows but does not saturate. The amount of initial decrease scales with the laser fluence and the stress crosses over to tensile above 220 mJ/cm^2. At 240 mJ/cm^2, only four laser shots are needed to fully relieve the average stress. The stress then continues to decrease, reaching a value of -2.7 GPa. To our knowledge, this is the highest tensile stress reported for a ta-C film. In contrast, the highest tensile stress that we have been able to achieve from furnace annealed films is ~-0.5 GPa. Otherwise, the laser annealed stress relief curves are very similar to those generated from furnace annealing [11]. No measurable change in thickness occurs, and the surface roughness as measured with an atomic force microscope is unchanged at < 1Å rms. Above 240 mJ/cm^2 the annealing behavior changes character. At 260 mJ/cm^2, the stress after initially rapidly decreasing actually starts to gradually become more compressive although the net stress remains tensile. At 280 mJ/cm^2 the switch from highly compressive to highly tensile and back to compressive is even more dramatic. As discussed below, these changes in behavior at high fluence are associated with a change in the structure to a more graphitic character. Importantly, all laser-annealed films remained adhered to the substrate with no visible changes until the highest fluences reached in this study.

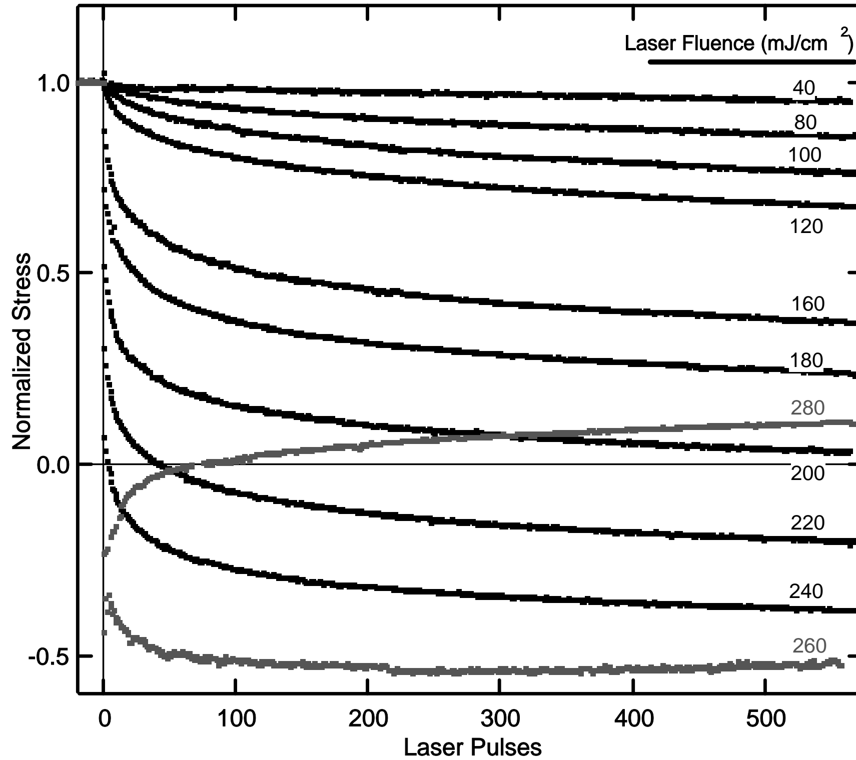

Fig. 4.2 Normalized stress vs. laser shots at varying fluence. Each point on the graph is measured after an applied laser pulse. The initial stress magnitude was 7.1±0.3 GPa. Above 240 mJ/cm^2 Raman spectra show significant increases in 3-fold bonding (see Fig. 4.4).

Effects of thickness

Fig. 4.3a is a plot of the stress relief after one laser shot versus fluence for four sample thicknesses. Below 120 mJ/cm^2 the data show very little stress relief; although examination of the data reveal that there is a small but measurable change in stress (≤ 1%). As the fluence increases above 120 mJ/cm^2, the total stress relief increases with a clear trend of increasing stress relief for decreasing sample thickness. For the 500 Å thick sample one laser shot at 240 mJ/cm^2 is sufficient to drive the average stress into the tensile regime. The thicker samples show considerably less relief.

Fig. 4.3b is a plot of the data for the same samples, but for further annealing to 500 laser shots. It is clear from this data that there is an effect on the stress even for the lowest fluence of 40 mJ/cm^2, and at the higher fluences all samples are driven near or into the tensile regime. Significantly, the trend of increasing stress relief with decreasing thickness and constant fluence remains.

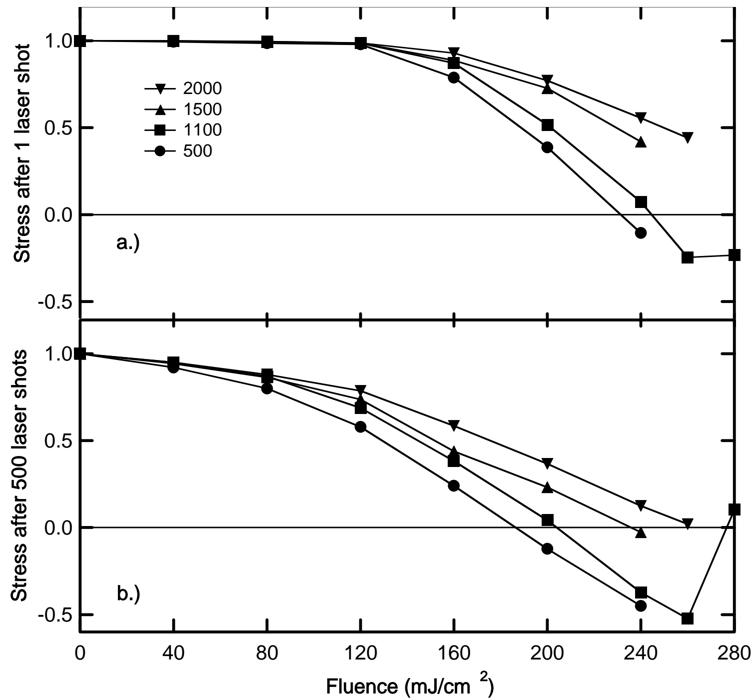

Fig. 4.3. The measured decrease in normalized stress vs. fluence after a.) 1 laser shot and b.) 500 laser shots for samples varying in thickness from 500 to 2000 Å.

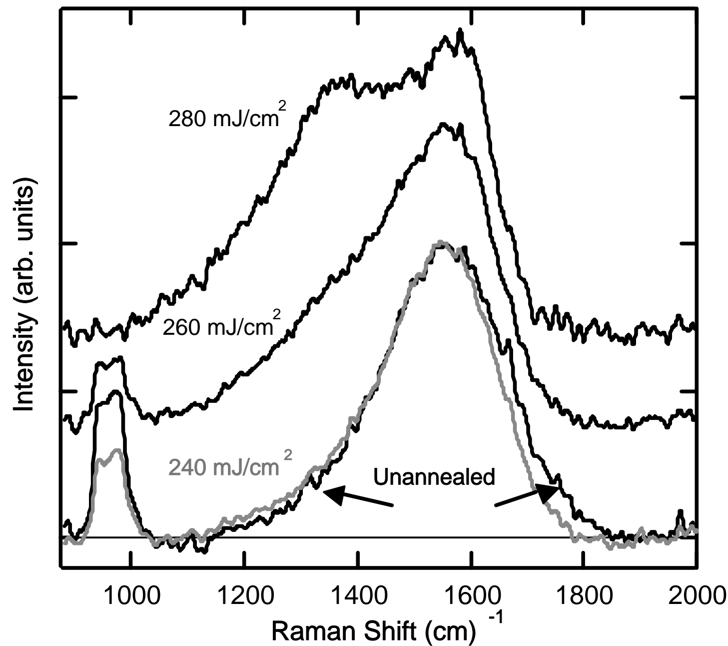

Fig. 4.4. Raman spectra of four samples annealed at varying fluence for 500 laser shots. Major bond changes occur for fluences above 240 mJ/cm^2. The sample annealed at 240 mJ/cm^2 has a tensile stress of 2.8 GPa.

Fig. 4.4 is a plot of the Raman spectra of an unannealed, 240, 260 and 280 mJ/cm^2 annealed samples from the 1100 Å thick samples shown in Fig. 4.2 after >500 laser shots. Comparing the unannealed spectra to the 240 mJ/cm^2 sample, the changes in the Raman spectra

with annealing are minor considering the stress has changed by almost 10 GPa. There is a narrowing of the main peak near 1560 cm^{-1} on the high frequency side with a small increase in intensity near 1350 cm^{-1}. In addition, there is a decrease in the intensity of the second order Si peak at 960 cm^{-1} indicating an increase in the optical absorption of the film. These changes imply an ordering of the 3-fold coordinated carbon and are very similar to those reported (see Sullivan et al. [10] fig. 2) for samples that were vacuum furnace annealed for 30 minutes at 600 °C. For the higher fluence samples shown in Fig 4.4, the Raman spectra for the two films are more significantly altered. There is a pronounced increase in intensity near 1370 cm^{-1} that increases with fluence and is indicative of graphitization of the ta-C thin film, presumably from the increased temperature at the higher fluences. The sample at 260 mJ/cm^2 has the highest sustained tensile stress of over –3.5 GPa, while the sample showing the highest intensity at 1370 cm^{-1} in the Raman spectra of Fig. 4.4, after an initial large tensile excursion, has gradually moved back to compressive stress with increasing laser shots.

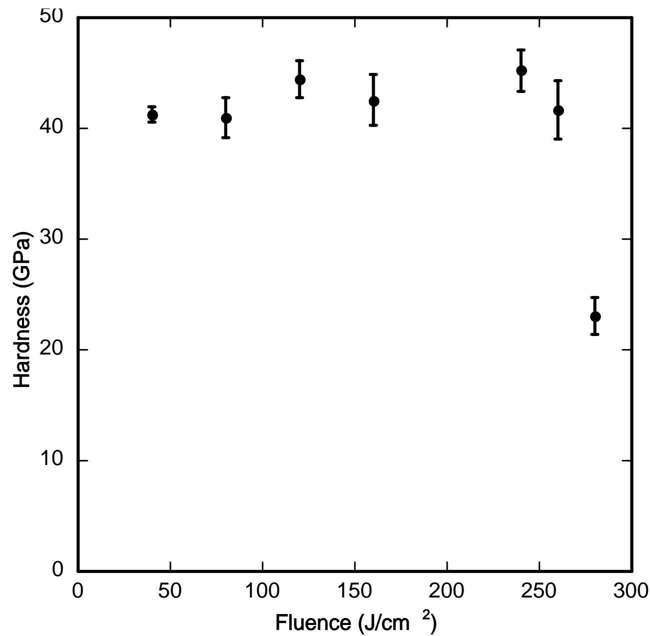

Fig. 4.5. Hardness vs. laser fluence for 1100 Å thick ta-C samples. Each sample was indented 24 times to a depth of 15 nm. The data points are the average hardness and the error bars represent one standard deviation.

Fig. 4.5 is a plot of the hardness vs. laser fluence for selected 1100 Å thick samples. The hardness is constant within the error of the measurement around 43 GPa. The only sample that shows a significant change in hardness is at the highest fluence of 280 mJ/cm^2 where the hardness drops to 23 GPa. This correlates well with the significant graphitization in the Raman spectra of Fig. 4.4. Interestingly, the sample at 260 mJ/cm^2 shows no change in hardness even though its Raman spectra shows evident though less graphitization. The data do not rule out a slight increase in hardness with fluence, similar to results reported for furnace annealed films [34,35]; however, the most straightforward interpretation is a constant hardness with annealing until the damage threshold is reached.

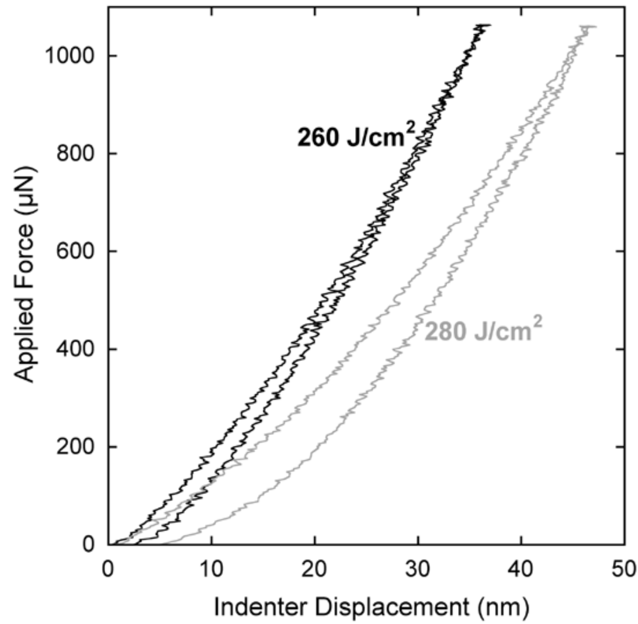

Fig. 4.6. Comparison of the load-displacement profiles for films annealed at fluences above and below the damage threshold.

To further illustrate the dramatic change in hardness as the laser fluence is increased above 260 J/cm^2, Fig. 4.6 compares the load-displacement profiles for indents just above and below this damage threshold. At a fluence of 260 J/cm^2, the maximum indenter depth at a load of 1060 μN was 37 nm, whereas at a fluence of 280 J/cm^2, the maximum depth was 47 nm. The contact depth, or depth of the residual impression after unloading, was 18 and 28 nm respectively.

One other important feature in the load-displacement profile is the presence of displacement excursions or "pop-in" events, the first of which occurs at a load of 2000 μN. This displacement excursion and associated residual impression after indentation is shown in Fig. 4.7. Discontinuous displacement excursions during in instrumented indentation have been associated with fracture/delamination events [36] and dislocation bursts [37,38] associated with the onset of plasticity. In some materials such as silicon, displacement excursions have also been associated with local pressure-induced phase transformations [39], although there is evidence in silicon to suggest that the phase transformations and the pop-in (or pop-out on unloading) events are independent [40]. Based on the image of the residual impression shown in Fig. 4.7, there appears to be evidence of a penny-shaped delamination zone emanating from each of the three sides of the indent, and no indication of radial or channel cracking emanating from the indent corners. The quantification of these displacement excursions and the connections to specific fracture/delamination events is the subject of ongoing research.

Fig. 4.8 is a plot of the calculated temperature versus time at varying depths into a 1000Å thick ta-C sample on Si (100) at a fluence of 250 mJ/cm^2 - the damage threshold as determined by Raman spectroscopy for this thickness. From the curves it is clear that the surface temperature is very high (~2500°C) at the end of the laser pulse. The maximum interface temperature (~900°C) occurs 5 nanoseconds later as the heat pulse travels into the sample - well below the melting point of crystalline Si (1410°C). The large temperature gradient (~1600°C) is driven by two factors. The first is the relatively low thermal conductivity of the ta-C (0.03 W/cmK)

compared to the Si (100) substrate (1.4 W/cmK at 25°C decreasing to 0.3 W/cmK at 900°C) that rapidly draws heat away from the interface. The second is the high absorption coefficient ($\alpha = 10^6$/cm) at 248 nm (5 eV) that concentrates 90% of the laser energy in the first ~250 Å at the film surface.

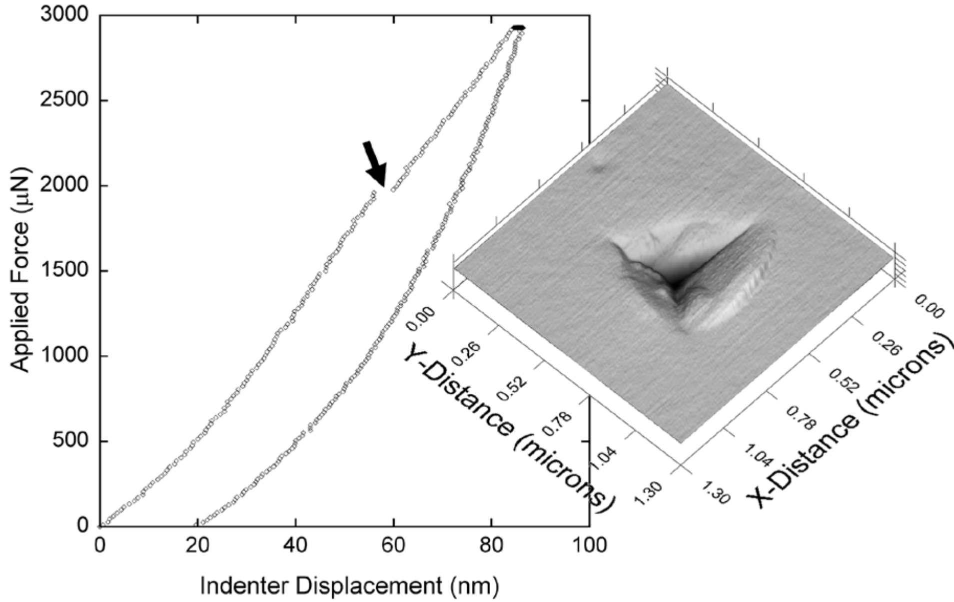

Fig. 4.7. Observed load-displacement curve to a maximum depth of ~ 85 nm, and quasi-AFM profile of the residual indent impression obtained by rastering the berkovich tip across the surface at a constant force. A displacement excursion or "pop-in" event was observed at 2000 μN, when the maximum depth was about half of the film thickness.

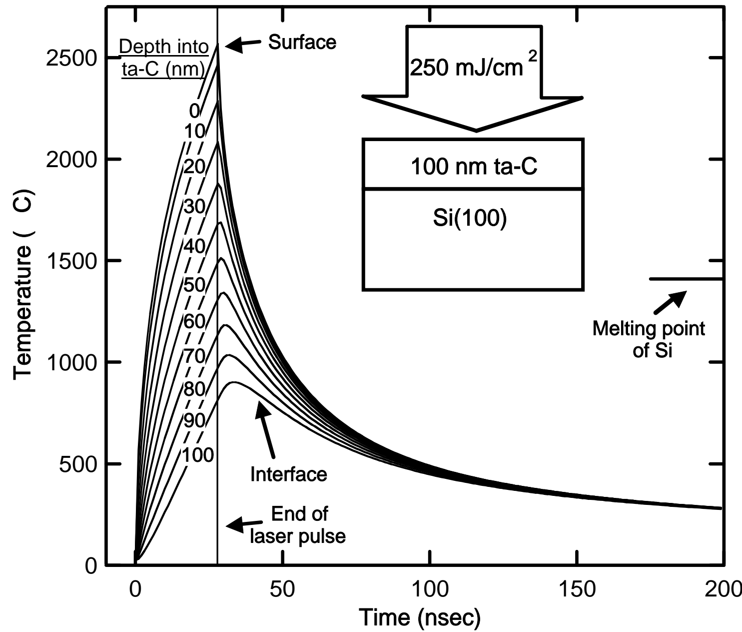

Fig. 4.8. FEM calculation of the temperature vs. time at varying depth for a 1000Å thick ta-C film on a Si (100) substrate irradiated with a 250 mJ/cm² 248nm laser pulse.

The FEM revealed that laser annealing at 248 nm produced high temperature gradients through the film thickness for all experimental conditions in this study. Fig. 4.9 is a plot of the maximum surface and interface temperature reached during the applied laser pulse as a function of fluence for the four experimental thicknesses annealed. For the 500 Å thick sample at a given fluence, the maximum surface temperature is lowest due to heat energy lost to the relatively nearby Si substrate; conversely, the interface temperature is highest of the four thicknesses due to its proximity to the surface. As the film thickness increases the surface temperatures increase while the interface temperatures decrease, and the maximum temperature gradients between the surface and interface increase. The interface temperature for the 500 Å thick sample at high fluence approaches the melting point of Si.

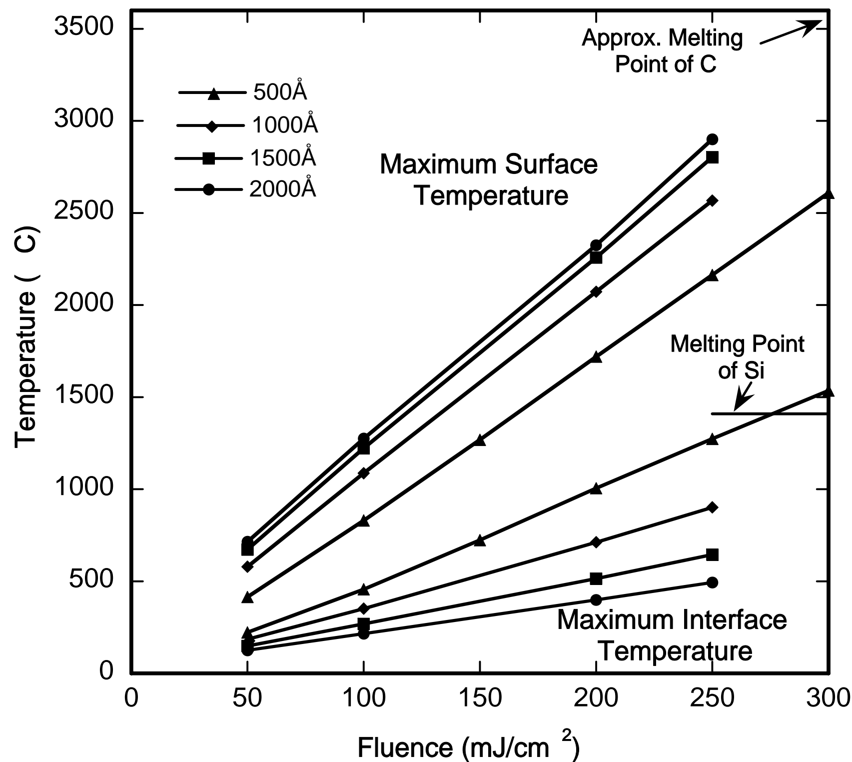

Fig. 4.9. Plot showing the maximum calculated temperature at the film surface and at the interface with the underlying Si substrate as a function of film thickness.

4.4 Discussion

The main difference between the furnace and laser annealed samples is the large tensile stresses generated in the films annealed at the higher fluences; and the high transient surface temperatures calculated for the laser annealing (>2000°C), much higher than the maximum stability temperature (~1100°C) of furnace annealed ta-C thin films [13,14,41].

There are at least four possible processes that can explain various aspects of the stress relief seen by laser annealing. First, is that heating at the carbon/silicon interface is causing carbide formation as reported by Majni et al. [26] Second, is the formation of nanocrystalline diamond and/or graphite due to the high temperatures reached by laser annealing. Third, is the same mechanism seen for furnace annealed films [12]; namely, a more subtle local- or medium-

range [42] ordering of both the 3- and 4-fold coordinated carbon without the appearance of long range order. Fourth, is graphitization of 4-fold regions.

Carbide formation

The degree of carbide formation will depend on the existing level of C/Si mixing, and the temperature and duration of the heat pulse near the interface. The pulsed laser deposition process used to grow the films can produce carbon ion energies in a broad range up to several hundred eV. This results in a mixing layer a few nanometers thick that will react to form carbides at temperatures near 900°C [43]. Fig. 4.9 shows that at the interface, the 500Å thick samples and the 1100Å thick samples at high fluence are at or above this temperature raising the possibility of carbide formation. The thin region of carbide at the interface would not account for the large changes in stress

Should the interface reach the melting point of Si (1410°C), it is possible that long-range diffusion could occur, as seen by D'Anna et al. [26,44], creating a SiC layer that is much thicker than the mixing layer. The interface temperature data from the model shown in Fig. 4.9 show that only the thinnest films reach high enough interface temperatures to melt the Si suggesting that very thick carbide formation has not occurred.

In either case, SiC formation would most likely generate tensile stresses consistent with the experimental data but it is probably not playing a major role under the conditions explored in this study.

Formation of nanocrystallites

The formation of diamond nanocrystallites is plausible, as the film is initially in a high state of compressive stress. The rapid heating to high temperatures could bring local areas of carbon in the film into the region of the phase diagram where diamond is the stable phase. Formation of diamond nanocrystallites would cause local regions to densify, and tend to produce net tensile stresses self-limiting the size of the crystals. Visible Raman scattering would not detect changes in the 4-fold bonded carbon due to the reduced sensitivity to 4-fold carbon (3-fold is resonantly enhanced) and the small crystal size. Arguing against this possibility is the lack of changes in hardness, thickness, surface morphology and reflectivity below the damage threshold.

Local- or medium-range ordering

For the low fluence laser-annealed samples, stress relief has many of the same characteristics as for furnace-annealed samples. For example, the kinetics of the laser annealing process appear similar (compare Fig. 4.2 to Fig. 1 of Sullivan et al. [11]). At a given laser fluence, the initial stress relief is comparatively large with smaller decreases after each subsequent laser pulse. The bonding changes below the damage threshold are also very similar to those found in furnace annealed samples (compare Fig. 4.4 to Fig. 2 of Friedmann et al. [10]), with no significant change in hardness till the onset of large-scale graphitization. Also, atomic-force microscopy scans of the film surface show no roughening. Taken together, these observations suggest that stress changes from laser annealing are in part due to the same mechanism operating for furnace annealing.

For thermal annealing, the stress relief mechanism is one of bond-breaking transformations that cause rearrangement of the carbon atoms in the ta-C structure that result in a net in-plane volume decrease and an ordering of both the 3- and 4-fold bonded carbon leading to stress relief with no measurable change in 4-fold content [12] and no increase in long range order. These bond transformations are thermally activated with the same kinetics as a first-order

chemical reaction; and the stress relief is sensitive to both the time and temperature history of the sample [11]. Temperatures in the laser annealed films are much higher than the 600°C used for furnace annealing, but for much shorter times (nanoseconds vs. minutes) resulting in a similar stress relief. Under these conditions, the high tensile stresses could be explained by further ordering of both the 3- and 4-fold carbon activated by the very high temperatures without the production of long-range order.

Graphitization

Above the laser damage threshold the samples show significant graphitization, reduced hardness, and a change from tensile back to compressive stress. The change back to compressive stress is in the direction expected for conversion of 4- to randomly oriented 3-fold coordinated carbon, as the volume of 3-fold coordinated carbon is greater than 4-fold due to the large -orbital.

It is possible that combinations of these processes contribute to the stress changes depending on the laser fluence. A detailed study of the microstructure will help decide the relative role of these mechanisms.

Implications for MEMS

The large temperature gradients calculated by the model for the laser annealing process are a problem for MEMS devices, as they can potentially lead to stress gradients in the films even though the average stress is very low. To test this, a portion of the silicon substrate of a laser annealed ta-C specimen was chemically etched away with acids. Upon release from the substrate the ta-C thin film curled strongly upward from the substrate indicating that there was a large strain gradient in the sample with the surface being under tension compared to the film near the bottom interface. This test needs to be repeated in a more systematic way before drawing detailed conclusions; nevertheless, it seems clear that strain gradients will be a problem for laser annealing. The temperature gradient is determined by the absorption coefficient for the wavelength of the laser light and by the proximity and thermal conductivity of the substrate. At wavelengths below the bandgap of Si it should be possible to more uniformly heat the film with little or no heat dissipation into the substrate. A lower absorption coefficient implies the laser pulse must be longer or higher in power to achieve the same temperatures reached in this study.

Laser annealing is a process that can be done over large flat areas with speeds that are technologically useful. (For example, excimer laser annealing is widely used to crystallize amorphous Si thin films in the production of large area thin-film transistor flat-panel displays.) As we have demonstrated, the measurement of wafer curvature can also be done rapidly and during laser annealing. This is an important tool for controlling average stress. Finally, it should be possible to periodically laser anneal a film during growth while monitoring the wafer curvature, as the stress relief is much faster (< 1 μsec) than any practical growth rate. In this manner a stress relieved film of any practical area and thickness can be grown. For protective coatings, the issue of strain gradients is not so important provided that the ta-C thin film remains slightly compressively stressed (tensile films crack more easily). For MEMS applications, it will be crucial to solve the problem of strain gradients.

4.5 Conclusions

Low laser fluence excimer laser annealing can fully relieve the average stress in ta-C thin films without causing significant changes in the film bonding and hardness. At high laser

fluences, dependent upon sample thickness, changes in the Raman spectra and hardness indicate damage to the film related to graphitization. Near the damage threshold (both above and below) it is possible to induce large tensile stresses (~ 3 GPa) in ta-C thin films. The nanoindentation force versus depth curves showed a series of "pop-in" events that were indicative of film cracking that correlated inversely in force with the measured tensile stress. Modeling of the laser-induced temperatures revealed that high surface temperatures (> 2000°C) and large temperature gradients are induced by the laser pulse. These gradients lead to nonuniform stress relaxation causing strain gradients through the thickness of the film.

4.6 References

1. J. P. Sullivan, T. A. Friedmann, and K. Hjort, Mrs Bulletin **26,** 309 (2001).
2. T. E. Buchheit, S. J. Glass, J. R. Sullivan, S. S. Mani, D. A. Lavan, T. A. Friedmann, and R. Janek, Journal of Materials Science **38,** 4081 (2003).
3. D. A. LaVan, R. J. Hohlfelder, J. P. Sullivan, T. A. Friedmann, M. Mitchell, and C. I. H. Ashby, Materials Research Society Symposium Proceedings **594,** 295 (2000).
4. D. A. LaVan, K. Jackson, B. McKenzie, S. J. Glass, T. A. Friedmann, J. P. Sullivan, and T. E. Buchheit, ASTM Special Technical Publication**,** 62 (2001).
5. I. Chasiotis, S. W. Cho, T. A. Friedmann, and J. P. Sullivan, in *Materials research society symposium proceedings*; *Vol. 795* (2004), p. 461.
6. J. R. Webster, C. W. Dyck, T. A. Friedmann, J. P. Sullivan, C. D. Nordquist, A. J. Carton, G. M. Kraus, and G. D. Schmidt, Proc. of SPIE **5344,** 71 (2004).
7. J. R. Webster, C. W. Dyck, J. P. Sullivan, T. A. Friedmann, and A. Carton, Electronics Letters **40,** 43 (2004).
8. B. E. N. Keeler, D. W. Carr, J. P. Sullivan, T. A. Friedmann, and J. R. Wendt, Optics Letters **29,** 1182 (2004).
9. D. W. Carr, J. P. Sullivan, and T. A. Friedmann, Optics Letters **28,** 1636 (2003).
10. T. A. Friedmann, J. P. Sullivan, J. A. Knapp, D. R. Tallant, D. M. Follstaedt, D. L. Medlin, and P. B. Mirkarimi, Applied Physics Letters **71,** 3820 (1997).
11. J. P. Sullivan, T. A. Friedmann, and A. G. Baca, J. Electr. Mater. **26,** 1021 (1997).
12. T. M. Alam, T. A. Friedmann, P. A. Schultz, and D. Sebastiani, Phys. Rev. B **67,** 245309 (2003).
13. R. Kalish, Y. Lifshitz, K. Nugent, and S. Prawer, Appl. Phys. Lett. **74,** 2936 (1999).
14. A. C. Ferrari, B. Kleinsorge, N. A. Morrison, A. Hart, V. Stolojan, and J. Robertson, Journal of Applied Physics **85,** 7191 (1999).
15. L. C. Nistor, J. Vanlanduyt, V. G. Ralchenko, T. V. Kononenko, E. D. Obraztsova, and V. E. Strelnitsky, Applied Physics a-Solids and Surfaces **58,** 137 (1994).
16. S. Prawer, R. Kalish, and M. Adel, Applied Physics Letters **48,** 1585 (1986).
17. T. V. Kononenko, V. I. Konov, V. G. Ralchenko, and V. E. Strelnitsky, Proceedings of the SPIE The International Society for Optical Engineering **1759,** 106 (1992).
18. K. S. Harshavardhan, R. S. Yalamanchi, and L. K. Rao, Appl. Phys. Lett. **55,** 351 (1989).
19. M. Bowden, D. J. Gardiner, and J. M. Southall, J. of Appl. Phys. **71,** 521 (1992).
20. V. Y. Armeyev, E. N. Loubnin, V. G. Ralchenko, and V. E. Strelnitsky, Appl. Phys. Lett. **58,** 2758 (1991).
21. N. I. Chapliev, T. V. Kononenko, A. A. Smolin, and V. E. Strelnitsky, Surface & Coatings Technology **47,** 730 (1991).

22. G. Dumitru, V. Romano, H. P. Weber, S. Pimenov, T. Kononenko, J. Hermann, S. Bruneau, Y. Gerbig, and M. Shupegin, Diamond and Related Materials **12,** 3 (2003).
23. G. Dumitru, V. Romano, H. P. Weber, S. Pimenov, T. Kononenko, M. Sentis, J. Hermann, and S. Bruneau, Applied Surface Science **222,** 1 (2004).
24. T. V. Kononenko, V. G. Ralchenko, E. D. Obraztsova, V. I. Konov, J. Seth, S. V. Babu, and E. N. Loubnin, Applied Surface Science **86,** 234 (1995).
25. S. Weissmantel, G. Reisse, and S. Schulze, Applied Surface Science **54,** 317 (1992).
26. G. Majni, P. Mengucci, E. Danna, G. Leggieri, A. Luches, and V. Nassisi, Applied Physics a-Materials Science & Processing **49,** 181 (1989).
27. G. G. Stoney, Proc. R. Soc. London, Ser. A **82,** 172 (1909).
28. J. A. Knapp, D. M. Follstaedt, S. M. Myers, J. C. Barbour, and T. A. Friedmann, J. of Appl. Phys. **85,** 1460 (1999).
29. P. Baeri and S. U. Campisano, in *Laser annealing of semiconductors*, edited by J. M. Poate and J. W. Mayer (Academic Press, New York, 1982), p. 75.
30. A. C. Ferrari, A. Libassi, B. K. Tanner, V. Stolojan, J. Yuan, L. M. Brown, S. E. Rodil, B. Kleinsorge, and J. Robertson, Physical Review B **62,** 11089 (2000).
31. C. H. Seager, T. A. Friedmann, and D. E. Bliss, in *Diamond for electronic applications*; *Vol. 416*, edited by D. Dreifus, A. Collins, C. Beetz, T. Humphreys, K. Das, and P. Pehrsson (Materials Research Society, Pittsburgh, 1996), p. 145.
32. A. J. Bullen, O. H. KE, D. G. Cahill, O. Monteiro, and A. vonKeudell, J. of Appl. Phys. **88,** 6317 (2000).
33. L. E. Fried and W. M. Howard, Phys. Rev. B **61,** 8734 (2000).
34. O. R. Monteiro, J. W. Ager, D. H. Lee, R. Yu Lo, K. C. Walter, and M. Nastasi, J. of Appl. Phys. **88,** 2395 (2000).
35. M. P. Siegal, D. R. Tallant, P. N. Provencio, D. L. Overmyer, R. L. Simpson, and L. J. Martinez-Miranda, Appl. Phys. Lett. **76,** 3052 (2000).
36. D. F. Bahr, C. L. Woodcock, M. Pang, K. D. Weaver, and N. R. Moody, International Journal of Fracture **119/120,** 339 (2003).
37. D. F. Bahr, D. E. Kramer, and W. W. Gerberich, Acta Materialia **46,** 3605 (1998).
38. J. Li, K. Van Vliet, T. Zhu, S. Yip, and S. Suresh, Nature **418,** 307 (2002).
39. H. S. Leipner, D. Lorenz, A. Zeckzer, H. Lei, and P. Grau, Physica B: Condensed Matter (Amsterdam) **308-310,** 446 (2001).
40. J. E. Bradby, J. S. Williams, and M. V. Swain, Phys.l Rev. B **67,** 085205 (2003).
41. T. A. Friedmann, K. F. McCarty, J. C. Barbour, M. P. Siegal, and D. C. Dibble, Appl. Phys. Lett. **68,** 1643 (1996).
42. X. Chen, J. P. Sullivan, T. A. Friedmann, and J. M. Gibson, Appl. Phys. Lett. **84,** 2823 (2004).
43. T. Kimura, H. Yamaguchi, L. Ji-Kui, S. Yugo, Y. Adachi, and Y. Kazumata, Thin Solid Films **157,** 117 (1987).
44. E. D'Anna, G. Leggieri, A. Luches, V. Nassisi, A. Perrone, G. Majni, and P. Mengucci, Mat. Chem. Phys. **23,** 433 (1989).

5.0 MEMS and NEMS Oscillators

5.1 Introduction

Micro-electro-mechanical systems (MEMS) [1], specifically, mechanical oscillators, are used in a wide variety of components, including filters for RF signals [2,3], sensors [4] for mechanical, electrical or magnetic forces, and detectors for chemical [5] and biological agents [6], etc. In many of these systems, the performance of the oscillator is limited by mechanical dissipation, Q^{-1} [7]. For example, in cantilever-based sensors for chemical or biological agents, the minimum detectable force on the cantilever, which often translates into the minimum amount of detectable analyte, scales as $Q^{-1/2}$, whereas for oscillators used as narrow bandpass filters in signal processing, the bandwidth of the filter is directly proportional to the internal dissipation in the oscillator, Q^{-1} [2,3]. Understanding processes that control internal dissipation is critical for these technologies, and this becomes increasingly important as new oscillator materials are introduced.

The oscillators described above and similar oscillators have been fabricated out of a variety of materials, ranging from those with a high degree of order, such as single crystal silicon, to materials exhibiting order in the tens of nanometers to over several hundred nanometers length scale, such as polysilicon, to materials exhibiting order on the scale of several nanometers, such as low temperature deposited silicon nitride, and to completely amorphous materials, such as silicon dioxide. Recently, tetrahedral amorphous carbon (ta-C) has been used in MEMS [8] and nano-electro-mechanical systems (NEMS) [9]. Tetrahedral amorphous carbon, which is sometimes also called amorphous diamond (a-D), is a purely amorphous carbon material consisting of approximately 80% 4-fold coordinated carbon and 20% 3-fold coordinated carbon [10].

In this section, we characterize mechanical dissipation in oscillators fabricated out of ta-C. The oscillators had dimensions as small as several tens of nanometers up to millimeters. The frequencies of these devices ranged from several kHz for the largest devices to several MHz for the smallest. The primary dissipation mechanism(s) were identified based on the observed quality factors and the measured or estimated mechanical and thermal properties of ta-C.

5.2 Theory

In any physical oscillator, three general classes of dissipation may be operative: extrinsic mechanical dissipation, intrinsic internal dissipation, and extrinsic internal dissipation. Extrinsic mechanical dissipation includes dissipation processes that are not inherent to the oscillator material but that occur due to either avoidable or unavoidable non-idealities in the design of the oscillator, e.g. clamping losses, or due to operation of the oscillator, e.g. air damping at high ambient pressures. Intrinsic dissipation mechanisms include those loss mechanisms that are inherent in every material, including ideal or defect-free materials. Extrinsic internal dissipation mechanisms include all dissipation processes that result from defects or disorder in a material, including point and extended defects, structural disorder, and defects associated with a free surface or boundary in the oscillator.

Extrinsic Mechanical Dissipation

The physical design of the oscillator may limit the mechanical dissipation independent of the oscillator material. Two of the most common mechanisms that may limit dissipation are clamping losses at the oscillator supports and air damping. Clamping losses depend sensitively on the oscillator design, with the losses being reduced by rigidly supporting the oscillator at a zero-displacement node of oscillation. In the case of a cantilever oscillator, some force will be transmitted necessarily to the supporting base of the oscillator. In this case, the clamping losses are reduced by making the oscillator more compliant, e.g. increasing the length, l, to thickness, t, ratio of the oscillator. Modeling of the effect of clamping losses on a cantilever oscillator gives a clamping-limited Q, $Q_{clamping}$, given by [11]

$$Q_{clamping} \approx 0.34\frac{l^3}{t^3}. \quad (5.1)$$

This estimate was made assuming a semi-infinite elastic body as the support. In the physical realization of a cantilever oscillator, supports with excessive compliance would be expected to decrease $Q_{clamping}$ further. To avoid being limited by clamping losses in a system with an intrinsic Q of 5×10^3, the ratio of l/t would need to be greater than 20.

Air damping may also limit the quality factor of real oscillators. At high pressures (above ~ 10 Pa), viscous drag results in a decrease in Q of more than 2 orders of magnitude. The exact dependence of Q on pressure, P, in this regime is dependent on the size of the oscillator and the width of the fluid boundary layer perpendicular to the direction of motion [12]. In the molecular flow regime, about 1 – 10 Pa, the quality factor is proportional to P^{-1} [12]. Below 0.1 Pa (< 1 mTorr), air damping was found to be insignificant for Si cantilever oscillators with dimensions of 10's to 100's of microns [12]. For practical purposes, measurements performed in vacuum of $< 1 \times 10^{-5}$ Torr will ensure that air damping is negligible for most oscillators.

Intrinsic Internal Dissipation

Intrinsic internal dissipation processes may be categorized into three separate mechanisms: dissipation due to electron-phonon interaction, thermoelastic dissipation, and dissipation due to thermal phonon-mechanical vibration interaction [13]. The electron-phonon dissipation arises from the viscous drag created by the response of free electrons in a material to the motion of the ions as they follow the mechanical oscillation. It is only a significant form of dissipation in materials in which the electrical conductivity is high, i.e. metals. For ta-C, the electrical conductivity is approximately 10^{-4} Scm^{-1}, which is several of orders of magnitude lower than that of most metals. Hence, this dissipation mechanism is not expected to be significant in this material.

Thermoelastic dissipation occurs as a result of the temperature gradients created in a material experiencing mechanical oscillations that are not volume-conserving, e.g. longitudinal vibrations in a bar or transverse bending vibrations in a beam. These oscillations cause local net compression or tension in the structure, inducing a local temperature change, ΔT, in proportion to the volume change, $\Delta T \sim (3\alpha)^{-1}\Delta V/V$, where α is the linear coefficient of thermal expansion. For systems in which the vibrational modes are volume conserving, e.g. those experiencing only pure shear modes or for longitudinal modes in certain materials that have a Poisson's ratio, ν, = 0.5, thermoelastic dissipation is not significant.

For systems that are limited by thermoelastic dissipation, the quality factor, Q_{TED}, may be estimated. In the case of longitudinal oscillations of a bar,

$$Q_{TED} = \frac{9C^2}{\kappa T \alpha^2 \rho \omega}, \tag{5.2}$$

where C is the heat capacity per unit volume, κ is the thermal conductivity, T is temperature, ρ is density, and ω is the vibrational angular frequency [14].

The case of transverse vibrations of a beam has been analyzed by Roszhart [15] with the resulting expression for Q_{TED},

$$Q_{TED} = \frac{1}{2\Gamma(T)\Omega(f)}, \tag{5.3}$$

with

$$\Gamma(T) = \frac{\alpha^2 TE}{4\rho C_p}, \tag{5.4}$$

and

$$\Omega(f) = \frac{2f/F_0}{1+(f/F_0)^2}, \tag{5.5}$$

where

$$F_0 = \frac{\pi\kappa}{2\rho C_p t^2}. \tag{5.6}$$

Here f is the oscillator frequency, E is the Young's modulus, F_0 is a characteristic frequency, C_p is the specific heat capacity, and t is the oscillator thickness. More recently, an exact expression for Q_{TED} in thin cantilever beams has been presented by Lifshitz and Roukes [16],

$$Q_{TED} = \frac{C}{E\alpha^2 T}\left(\frac{6}{\xi^2} - \frac{6}{\xi^3}\frac{\sinh\xi + \sin\xi}{\cosh\xi + \cos\xi}\right)^{-1}, \tag{5.7}$$

where

$$\xi = t\sqrt{\frac{\omega\rho C_p}{2\kappa}}. \tag{5.8}$$

In most situations, Q_{TED} calculated either from equations 5.3 or 5.6 are in close agreement. In real systems, e.g. Si cantilever oscillators ≥ 10 μm thick, Q's limited by thermoelastic dissipation have been observed [15]. However, for the thinner, ≤ 2.3 μm, cantilevers fabricated from Si and silicon nitride that are more typical of MEMS, the quality factors were found to be lower than the predicted limits of thermoelastic dissipation [17,18].

In the estimates for Q_{TED}, presented above, it was assumed that the oscillator critical dimensions (bar length in a longitudinal oscillator or beam thickness for a cantilever oscillator) exceed the phonon mean free path so that thermal transport is well-described by diffusive phonon transport. As oscillator dimensions decrease, ballistic phonon transport dominates. Qualitatively, this increases the apparent thermal conductivity across the short dimension of the oscillator, resulting in a decrease in Q_{TED}.

In the absence of thermoelastic dissipation and in materials of low electrical conductivity, dissipation may be controlled by the interaction of thermal phonons with the mechanical vibrations of the oscillator. This dissipation mechanism originates from the perturbation of the local thermal phonon population due to the propagating mechanical vibration. Mechanical energy is dissipated as the phonon population readjusts to its thermal equilibrium. An estimate for the limiting quality factor associated with this dissipation mechanism, Q_{ph}, is given by [13],

$$Q_{ph} \approx \frac{\rho v^2}{C T \gamma^2}\left[\frac{\omega \tau_{ph}}{1+(\omega \tau_{ph})^2}\right]^{-1}, \tag{5.9}$$

where v^2 is the sound velocity, γ is the Gruneisen's constant, and τ_{ph} is the phonon relaxation time. The phonon relaxation time can be calculated from the longitudinal and transverse velocities of sound in the material, from the following equation,

$$\tau_{ph} = \frac{3\kappa}{\rho C_p v_D^2}, \tag{5.10}$$

where v_D is the Debye sound velocity, which is defined by the following equation:

$$\frac{3}{\upsilon_D^3} = \frac{1}{\upsilon_l^3} + \frac{2}{\upsilon_t^3}, \tag{5.11}$$

here, v_l and v_t are the velocity of longitudinal and transverse sound waves in the material, respectively. The longitudinal sound velocity is given by

$$\upsilon_l = \left(\frac{E}{\rho}\right)^{\frac{1}{2}} \tag{5.12}$$

For amorphous materials, the transverse sound velocity can be estimated as [19]

$$v_l = 1.65\ v_t. \tag{5.13}$$

For all of the intrinsic dissipation mechanisms discussed, and at frequencies well below the dissipation maximum, Q decreases linearly with increasing frequency ($\propto \omega^{-1}$). Hence the product, ωQ, should remain roughly constant. Since Q is simply related to the damping rate of the mechanical vibrations of a viscously damped oscillator,

$$Q = \frac{\omega}{2\delta}, \tag{5.14}$$

where δ is the damping rate which may be defined by considering the equation of motion for a point on an oscillator experiencing a particular vibrational mode,

$$x(t) = x_0 \exp(-\delta t)\cos(\omega t + \phi), \tag{5.15}$$

here $x(t)$ describes the amplitude at a particular point on the oscillator, then the constancy of ωQ is assured if δ is independent of oscillator frequency.

Extrinsic Internal Dissipation

In most real oscillators, the internal dissipation is not limited by intrinsic internal dissipation mechanisms. Instead, the dissipation is limited by defects within the oscillator or at the oscillator surfaces. Most of these extrinsic dissipation mechanisms are associated with structural reconfiguration or atomic motion between equilibrium or metastable states. In crystalline materials, many defect-related dissipation mechanisms have been described: dissipation due to the motion of vacancies or substitutional impurities, interstitial motion (e.g. Snoek relaxation), solute reordering in a solid solution (e.g. Zener relaxation), dislocation motion, grain boundary sliding, and eddy currents or domain motion in ferromagnetic or ferroelectric materials [20]. Characteristically, these defect processes give rise to a resonant or Debye-like relaxation of the form,

$$Q_{defect} = A\left[\frac{\omega\tau^*}{1+(\omega\tau^*)^2}\right]^{-1}, \tag{5.16}$$

where A is a constant related to the concentration and nature of the defect and τ^* is the relaxation time for the defect motion. In this form of dissipation, the quality factor of the oscillator exhibits a minimum at the frequency in which $\omega\tau^* = 1$, and this has been observed in a great variety of crystalline materials [20]. Furthermore, since many of these defect-related dissipation processes involve atomic motion, the relaxation time typically follows an Arrhenius relationship,

$$\frac{1}{\tau^*} = \frac{1}{\tau_0}\exp\left(\frac{-E_A}{k_B T}\right), \tag{5.17}$$

where $1/\tau_0$ is the characteristic atomic vibration frequency, on the order of 10^{13} Hz, E_A is the activation energy for the relaxation process, and k_B is Boltzmann's constant.

For many defect-related dissipation processes the activation energy for the dissipation process is close to the activation energy for self-diffusion in the material, typically 1 – 2 eV [20].

This arises naturally from the fact that many defect relaxation processes involve diffusive atom transport. For a 1 eV activation energy, a minimum in Q would be observed at about 300°C for a 1 kHz oscillator.

Another form of extrinsic internal dissipation is related to dissipation at the interfaces of the oscillator, especially at the oscillator surface. In some systems, particularly for small Si oscillators, losses due to surface dissipation may dominate the total measured dissipation [18,21]. The surface may be a source of atomic defects leading to high defect-related dissipation, or, as is the case with Si, the surface may be covered with a lossy material, such as amorphous SiO_2, that causes a decrease in quality factor as it grows on the surface [22]. For a cantilever geometry, the quality factor of the surface, Q_{surf}, covered with a lossy material of thickness, d, elastic modulus E_s, and characteristic dissipation = $1/Q_s$ is given by

$$Q_{surf} \approx \frac{tE}{6dE_s} Q_s, \tag{5.18}$$

where t is the oscillator thickness and E is the Young's modulus for the oscillator material, not including the surface. In this case, the measured quality factor would be $Q_{bulk}Q_{surf}/(Q_{bulk} + Q_{surf})$, where Q_{bulk} is the quality factor of the oscillator in the absence of the surface layer.

5.3 Oscillator Design

In an attempt to determine the dissipation mechanisms in ta-C, three oscillator designs were fabricated and analyzed: beams clamped rigidly at one end with an out-of-plane transverse vibration mode, beams supported at the nodes of an in-plane transverse vibration and beams rigidly clamped at one end with an in-plane transverse vibration mode. The geometries of the beams and their supporting structures were chosen in an attempt to eliminate extrinsic mechanical dissipation mechanisms. The dimensions of the three beam structures and their relation to the different dissipation mechanisms will be discussed in this section.

We modeled the transverse vibrations of all three prismatic beam designs using standard beam theory [23]. This yielded the following equation for the resonant frequency of the oscillators:

$$f_1 = \frac{c^2}{2\pi}\frac{t}{l^2}\sqrt{\frac{E}{12\rho}} \tag{5.19}$$

where f_1 is the resonant frequency of the first mode of oscillation, c is a constant determined by the boundary conditions of each beam design, t and l are the thickness and length of the oscillator, respectively, and E and ρ are the Young's modulus and the density of the ta-C material, respectively.

For the first set of beams, using the boundary conditions that the beams were free on one end and rigidly clamped on the other in an out-of-plane transverse vibration (cantilever), the constant, c, in equation 5.19 was determined to be 1.875 [23]. As can be seen from the schematic in Fig. 5.1a, the length, l, width, w, and thickness, t, of the beam lie along the x, y and z directions, respectively. The arrow indicates that the vibration of the cantilevers was transverse to the width and length, in the x-z plane. Cantilevers were defined with optical lithography and

fabricated with a thickness of 1.08 μm, a width of 10 μm and varying lengths of 100, 200, 350, 500, 800 and 1000 μm, with predicted resonant frequencies of 260, 65.1, 21.2, 10.4, 4.07 and 2.60 kHz, respectively. A plan view scanning electron micrograph (SEM) of a 350 μm long cantilever can be seen in Fig. 5.1b. To calculate these frequencies, a value of 680 GPa and 3.05 g/cm^3 were used for the Young's modulus and density of ta-C, respectively. The high aspect ratios of length to thickness were chosen so that the quality factors of the devices would not be limited by theoretical clamping losses (Eq. 5.1).

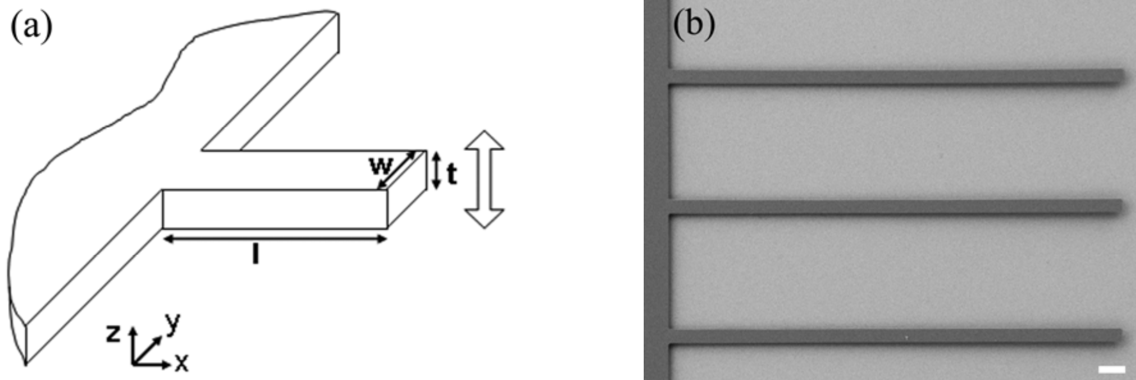

Fig. 5.1. (a) Schematic of the out-of-plane cantilever showing the dimensions and orientation of the cantilever. The arrow indicates the transverse vibration of the cantilever in the x-z plane. (b) An overhead, plan-view SEM of three cantilevers 350 μm long, 10 μm wide and 1.08 μm thick. The scale bar corresponds to 20 μm.

The second beam design, beams supported at nodes of an in-plane transverse vibrational mode, was designed in the fashion of Hsu *et al.* [24]. This design consists of two coupled beams. The primary beam oscillates in-plane while the supporting beams suspend the primary beam above the surface of the silicon wafer. As can be seen from Fig. 5.2a, the primary and support beams have lengths, l_p and l_s, thicknesses, t_p and t_s, and widths, w_p and w_s, respectively. For the primary beam, the length, thickness and width lie in the x, y and z directions, respectively, while for the support beams, the length lies along the x direction, while the width and thickness lie along the y and z directions, respectively. The primary beams were defined with e-beam lithography and fabricated with w_p = 1 μm, t_p = 0.5 μm and different lengths, l_p = 100, 200 and 300 μm. A plan view SEM of the device can be seen in Fig. 5.2b. The boundary conditions used to determine the resonant frequencies of the primary beams were such that both ends were free to translate in the x-y plane. This yields a value of 4.730, for the constant, c [23], with predicted resonant frequencies of 767, 200, and 88.7 kHz for the respective lengths using the same values for the Young's modulus and density of ta-C as for the cantilever structures.

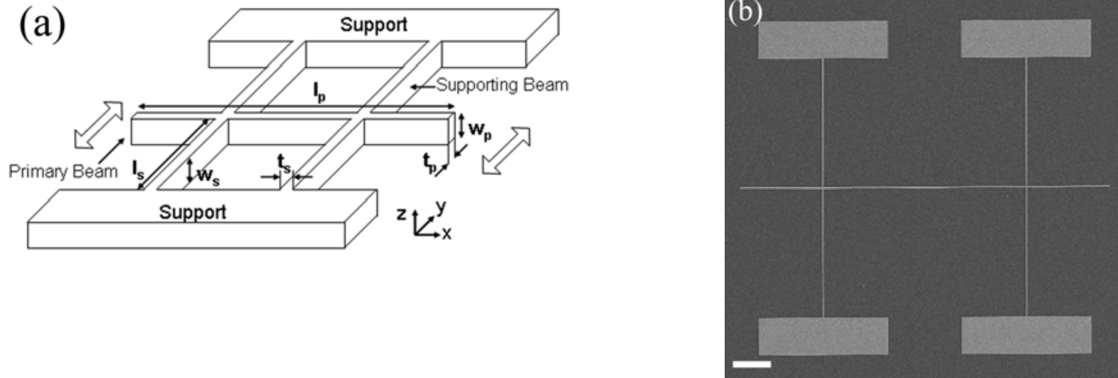

Fig. 5.2. (a) Schematic of the in-plane oscillator showing the dimension of the primary and support beams. The arrow indicates the in-plane (x-y plane) transverse vibration of the beam. (b) An overhead, plan-view SEM of the in-plane oscillators. The scale bar corresponds to 10 μm.

The positions where the supporting beams attach to the primary beam were chosen to lie at the nodes of the fundamental vibrational mode of the primary beam. Therefore, clamping losses for the primary beams should be less than those predicted for the cantilever beams used in the first design because the displacement of the primary beam at the nodes was nominally zero. Minimization of the displacement should limit the energy transferred into the supporting structures, thus decreasing the energy lost per vibration and increasing the quality factor. The supporting beams were also defined using e-beam lithography and fabricated with w_s = 1 μm, t_s = 0.25 μm and varying l_s = 35.36, 70.72 and 106.08 μm, with respect to the 100, 200 and 300 μm lengths of l_p.

For the third beam design, an in-plane transverse vibration of a cantilever, the same boundary conditions as for the out-of-plane transverse vibration were used to obtain the same result of 1.875 for the constant, c [23]. As can be seen from the schematic in Fig. 5.3a, the length, l, thickness, t, and width, w, of the beam lie along the x, y and z directions, respectively. These beams were defined using e-beam lithography and fabricated with w = 1 μm, two different thicknesses, t = 75 and 150 nm, with length, l = 8.35 μm. Arrays of these cantilevers were produced as can be seen from Fig. 5.3b, an SEM image of the cantilevers viewed at an angle. The resonant frequencies for the devices of width 75 nm and 150 nm were predicted to be 2.66 and 5.32 MHz, respectively. Again, the ratios of length to thickness were chosen to be large to reduce clamping losses. Since these structures oscillate in-plane, the support for the cantilevers should have been more rigid than for the out of plane oscillation because the in-plane oscillations perceive an almost infinitely thick and rigid support, while the out of plane oscillations perceive a support equal to the thickness of the film attached to only a semi-infinite support, the wafer.

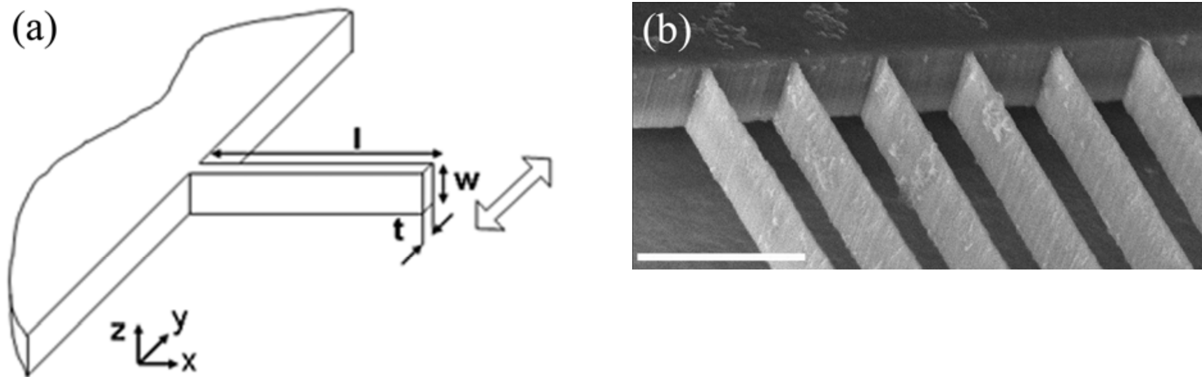

Fig. 5.3. (a) Schematic of the in-plane cantilever showing the dimensions and orientation of the cantilever. The arrow indicates the transverse vibration of the cantilever in the x-y plane. (b) A tilted-view SEM of cantilevers 1 μm wide, 8.35 μm long and 75 nm thick, with an in-plane oscillatory mode. The scale bar corresponds to 1 μm.

5.4 Device Fabrication

All the oscillators used in this study were surface micromachined on silicon wafers [25]. The different oscillators were fabricated using a similar process flow, with some devices defined using optical contact lithography and others defined using e-beam lithography. First, the shapes of the oscillators were defined using lithographic methods into a layer of resist on top of the ta-C material, as can be seen in Fig. 5.4(a). Then metal lift-off was performed to deposit a mask for the subsequent plasma etching. Using electron beam evaporation, 10 nm of titanium and 70 nm of aluminum were deposited on top of the wafer. Then the respective resists were removed using their appropriate solvents [Fig. 5.4(b)]. After this, the ta-C was etched in an oxygen plasma, at a flow of 30 sccm of O_2 and a pressure of 30 mTorr, using 400W of DC power [Fig. 5.4(c)]. The etch rate of ta-C in this plasma chemistry was approximately 40 nm/min. Next, the polysilicon was wet etched using a 0.2% HF in HNO_3 mixture. Additionally, the HF in the solution removes the aluminum from the surface. To fully release the devices, the silicon dioxide was etched in a 20% solution of HF in deionized water [Fig. 5.4(d)]. Any polysilicon remaining on the backside of the devices was wet etched in the 0.2% HF in HNO_3 solution. After thoroughly rinsing in water, the devices were rinsed in isopropyl alcohol and blown dried with nitrogen. They were then heated to 400°C for 1 minute in an argon atmosphere using rapid thermal annealing to remove any residual moisture from the devices. None of the oscillator structures exhibited auto-adhesion effects; therefore, super critical CO_2 drying or other release methods were not necessary. For some of the devices, a metal layer was deposited on the surface of the device supports to aid in electrical contact. None of the metal was deposited on the surface of the oscillators.

By tailoring the pressure and power of the oxygen plasma etch, different sidewall profiles were obtained. The etch parameters given above produce straight sidewalls as can be seen in a cross-sectional scanning electron micrograph (SEM) of an etched ta-C structure (Fig. 5.5). Higher pressure and lower power tend to produce undercutting of the masking material resulting in sloped sidewalls.

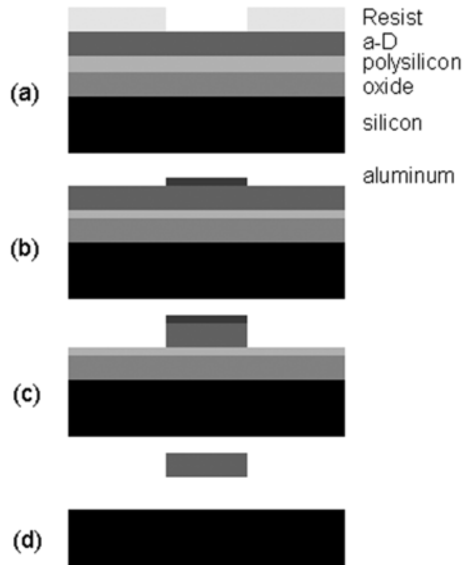

Fig. 5.4. Schematic showing the fabrication of the diamond oscillators. (a) E-beam or photolithographic patterning of photoresist to define the oscillator structure. (b) Metal evaporation and lift-off of resist to define the metal mask for the plasma etch. (c) Etching of the diamond material in an oxygen plasma. (d) Release of the device using diluted HF in HNO_3 to etch the polysilicon, and HF to etch the underlying silicon dioxide. No supercritical CO_2 drying was necessary to release the devices.

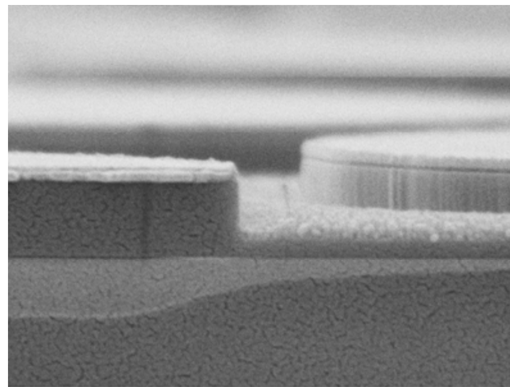

Fig. 5.5. Scanning electron micrograph showing the sidewalls produced by etching of ta-C in an oxygen plasma. The structures consist of cylinders etched into ta-C. The top layer is the aluminum mask used to define the shape of the structure.

5.5 Measurement

Two optical techniques were used to measure the resonant frequency of the oscillators. The out-of-plane vibrations of the cantilevers were measured using laser deflection techniques, while the in-plane vibrations of both the free-free beams and the cantilevers were measured by monitoring the intensity of the reflected laser light impinging at normal incidence on the devices. All devices were measured under vacuum conditions less than 10^{-5} Torr.

The laser deflection apparatus, used to measure the out-of-plane cantilevers, was similar to ones used in atomic force microscopy. A laser was focused onto the end of a cantilever, and the reflected light was directed into a photodiode. A schematic of the deflection setup used to measure the out-of-plane cantilevers can be seen in Fig. 5.6. Laser light was passed through a lens, which caused the beam to diverge. It was then sent through another lens to focus the light. As the light was converging, it was reflected off a mirror, through the vacuum window and focused onto an oscillator on the sample. (The vacuum components are not shown in the schematic.) The reflected light from the sample was sent to a split photodetector and was

positioned on the photodetector to minimize the voltage difference, A-B, between the detector's two halves. The A-B voltage was then routed into a spectrum analyzer that both synchronously drove the piezo element that mechanically shook the oscillator and recorded the A-B signal from the photodetector at the driving frequency. All measurements were made using the smallest resolution bandwidth on the spectrum analyzer to prevent broadening of the peaks from the spectrum analyzer, itself. Additionally, the minimum driving voltage needed to create a signal to noise ratio of approximately 10 to 1 was used to avoid any broadening of the peak due to non-linear driving. The frequency spectrum of the oscillators appeared symmetric about the peak over the frequency span of the measurements.

The in-plane oscillators were measured by monitoring the reflected laser intensity from a normal incident laser on the oscillators. A schematic of the setup can be seen in Fig. 5.7. The diameter of a collimated laser beam was expanded through the use of a beam expander to back illuminate a long working distance microscope objective. The objective focused the laser light down to a single point on the oscillator(s). The reflected signal was then sent back through the microscope objective into the beam splitter and finally to a photodetector. The electrical output from the photodetector was routed into the spectrum analyzer. For the in-plane free-free beams, the actuation was achieved using the same method as described above; the spectrum analyzer synchronously drove the piezo element and monitored the output from the photodetector. The in-plane cantilevers were driven by electrostatic actuation from the output of the spectrum analyzer. As opposed to the out-of-plane cantilevers, which produced a large signal reflected off the oscillator itself, the sizes of the in-plane oscillators do not produce large reflected components. Instead, in-plane optical interference [26] and light scattering modulate the intensity of the reflected laser light. For small oscillations, the magnitude of the modulation coincides with the amplitude of the oscillator motion, yielding the spectral response of the oscillator to the frequency of the applied actuation voltage. Similar to the actuation described above, the minimum driving voltage required to produce a significant signal to noise ratio was used to drive the oscillators. Also, the smallest possible resolution bandwidth on the spectrum analyzer was used to prevent broadening of the spectrum caused by the measurement, itself.

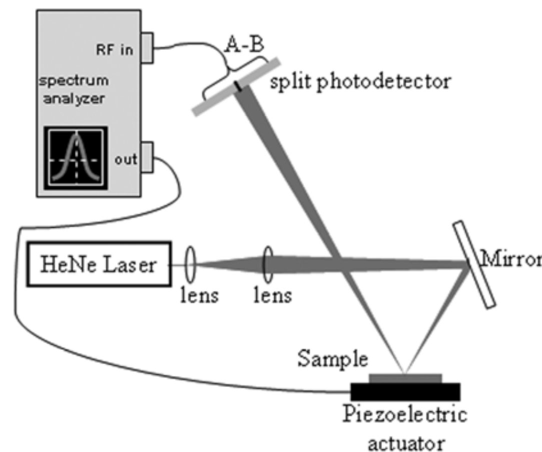

Fig. 5.6. Schematic showing the laser deflection technique used to measure the out-of-plane transverse vibrational mode of cantilevers. The spectrum analyzer outputs a signal to the piezoelectric element while monitoring the differential signal from the split photodiode at the same frequency as the driving output signal.

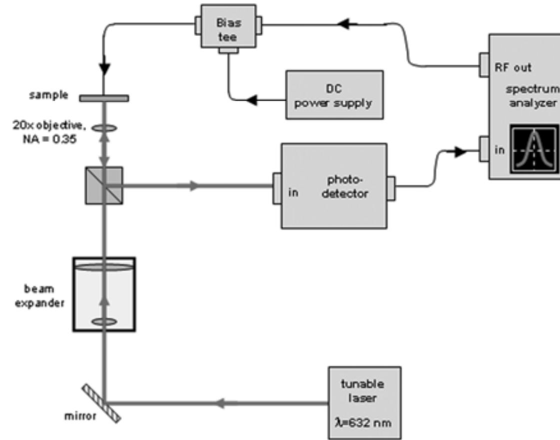

Fig. 5.7. Schematic showing the setup used to measure the in-plane transverse vibrational mode of cantilevers and beams. The spectrum analyzer outputs a signal to the piezoelectric element (or electrostatic actuation electrodes for some devices) while monitoring the intensity of the photodiode at the same frequency as the driving output signal.

5.6 Results and Discussion

For a given size oscillator, frequency spectra typically were recorded on at least five separate oscillators on the same wafer. The resonant frequencies and quality factors were determined from a least squares fit to a Lorentzian curve of the square of the linear voltage output of the spectrum analyzer (see inset of Fig. 5.8). For this particular curve, the resonant frequency is 20.074 kHz with a full width at half maximum value of 3.88 Hz and a quality factor of 5174. For each oscillator size, both the resonant frequencies and quality factors were averaged and standard deviations were calculated. A plot of the resonant frequencies of the out-of-plane cantilevers versus cantilever length can be seen in Fig. 5.8. From Eq. 5.19 we see that the resonant frequency varies as the inverse length squared; therefore, a least squares fit of an inverse square function was fit to the frequency versus length data. From this curve fit, the Young's modulus of the material was calculated to be 631 ± 64.9 GPa using a density of 3.05 ± 0.1 gm/cm^3 and a cantilever thickness of 1.08 ± 0.05 μm. The Young's modulus and other material's properties of ta-C are summarized in Table 5.1. For those constants that we did not directly measure or for which well established literature values could not be obtained, estimates were used assuming material's properties intermediate between diamond and graphite.

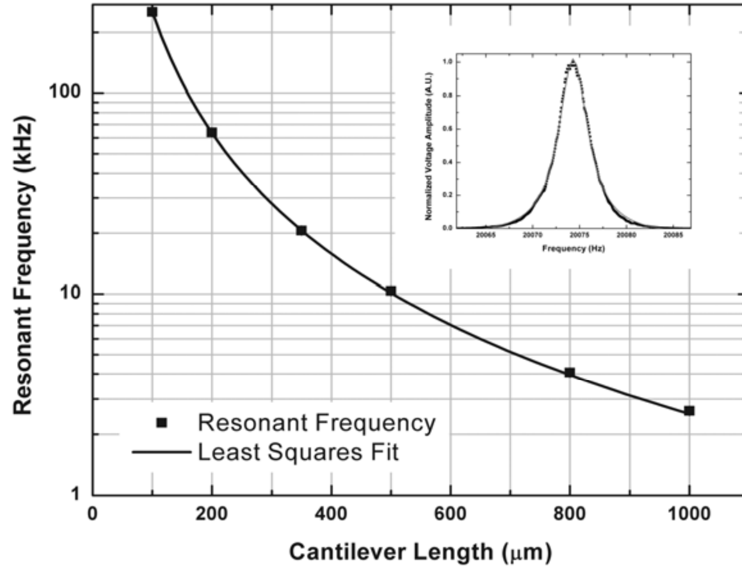

Fig. 5.8. Plot of the resonant frequency versus length for cantilevers made from a 1.08 μm thick ta-C film. Also shown is a least squares fit to an inverse square function. From this fit, the Young's modulus was determined to be 631 ± 65 GPa. The inset shows a least squares fit of a Lorentzian function to the frequency spectra of a cantilever.

Table 5.1. *Table of the mechanical and thermal properties of ta-C used in this study. For those constants that we did not directly measure or for which well established literature values could not be obtained, estimates were used assuming material's properties intermediate between diamond and graphite.*

Material Property	Value	Units
Heat Capacity per unit Volume (C)	1.83×10^6	(J / m^3 K)
Thermal Conductivity (κ)	3	(W / m K)
Density (ρ)	3050	(kg / m^3)
Young's Modulus (E)	631	(GPa)
Specific Heat Capacity (C_p)	600	(J / kg K)
Gruneisen's Constant (g)	1.37	none
Thermal Expansion Coefficient (α)	1.67×10^{-6}	(K^{-1})

Various possible sources of mechanical damping were considered for the oscillator structures studied here. The first damping mechanism we considered was clamping losses, which were estimated from Eq. 5.1. A plot of the maximum Q allowed by clamping losses, $Q_{clamping}$, versus resonant frequency is plotted in Fig. 5.9. We found that the measured Q of the oscillators was well below the theoretical limit imposed by clamping losses for all of the structures studied. This was primarily a result of the large ratios of cantilever lengths to thicknesses used in both the in-plane (ratios greater than 55:1) and out-of-plane (ratios greater than 90:1) cantilevers. Additionally, we would expect that $Q_{clamping}$ for the in-plane cantilevers would be larger than the limit established by the simulations of Hosaka *et al.* [11] because the in-plane cantilevers experience supporting structure both above and below the cantilever (full infinite plane support),

while Hosaka *et al.* modeled supporting structure only below the cantilever (half infinite plane support).

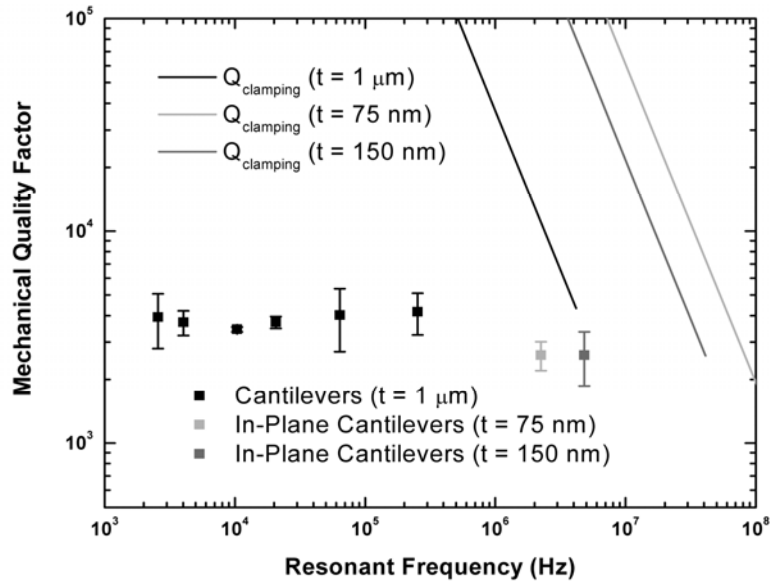

Fig. 5.9. Plot of the quality factor versus resonant frequency for a variety of cantilever oscillators. Also shown on the graph is a plot of the theoretical maximum value of quality factor due to clamping losses for the different cantilever designs. The shading of the 3 lines corresponds to the maximum value of Q for the data of the same shading.

The second damping mechanism we considered was air damping. The devices were measured in vacuum at pressures below 10^{-5} Torr, a pressure lower than the start of the molecular flow regime; therefore, we would not expect significant losses related to air or squeeze film damping [12]. Also, because the quality factors for vastly different sized devices are fairly similar, there did not appear to be any limiting Q that matches functionally to the mechanisms proposed by Blom *et al.* [12].

Next we considered an intrinsic dissipation mechanism, thermoelastic dissipation, that would place a limit on the value of Q, Q_{TED}, dependent on the oscillator material. The characteristic frequency for Q_{TED} (Eq. 5.6) varies inversely with oscillator thickness; therefore, the different oscillators that we fabricated had vastly different characteristic frequencies. These oscillator dimensions are summarized in Table 5.2. A plot of the measured quality factor versus the ratio of resonant frequency to characteristic frequency can be seen in Fig. 5.10. As the resonant frequency of an oscillator approaches its characteristic frequency, Q_{TED} decreases toward a minimum near 1 (Fig. 5.10). However, from this figure we can also see that the value of Q_{TED} is well above the experimental values of Q, which indicates that the quality factors were not limited by thermoelastic dissipation.

Table 5.2. *Table shows the characteristic frequency for the different oscillators, as calculated from Eq. 5.6. The characteristic frequency contains information regarding the heat flow through the oscillator and is dependent on material properties and oscillator physical dimensions.*

Oscillator	Transverse Direction	Thickness	Characteristic Frequency
Cantilever	out-of-plane	1 μm	2.21 MHz
Free-Free Beam	in-plane	500 nm	8.83 MHz
Cantilever	in-plane	150 nm	114 MHz
Cantilever	in-plane	75 nm	458 MHz

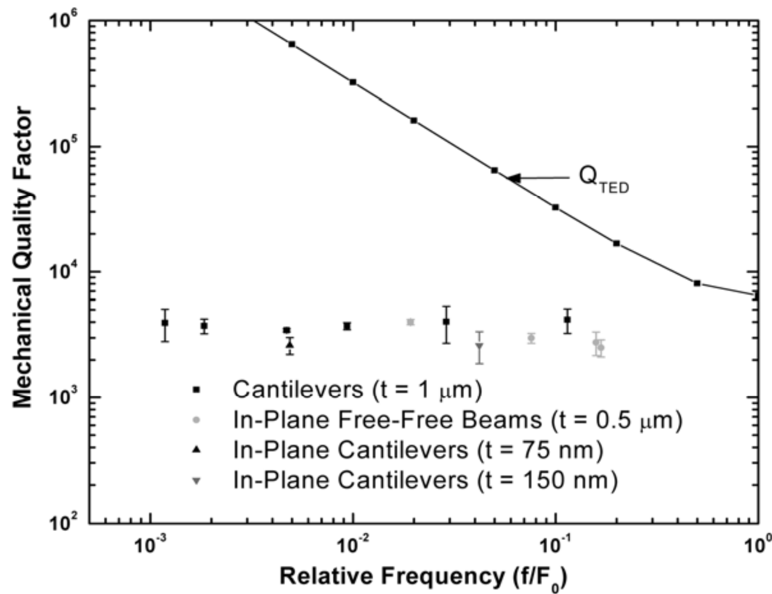

Fig. 5.10. Plot of the quality factor of ta-C oscillators versus the ratio of frequency to characteristic frequency. The solid line shows the theoretical maximum value of quality factor if the dissipation was limited by thermoelastic dissipation in the oscillators.

Since thermoelastic dissipation did not appear to be limiting the quality factor of the oscillators, the effects of phonon-mechanical vibration interactions were examined. By using Eqs. 5.11-5.13, along with the materials properties of ta-C in Table 5.1, we calculated the Debye speed of sound to be 1×10^5 m/s, giving a phonon relaxation time of 4.92×10^{-11} s. Using equation 5.10, we plotted the frequency dependence of the limiting quality factor for phonon-mechanical vibration interaction on Fig. 5.11. The limiting quality factor for these interactions is orders of magnitude larger than that measured in our experiments and is decreasing with increasing frequency. By comparing the measured quality factors and the theoretical quality factor limit, we assert that the quality factor of the oscillators was not limited by phonon-mechanical vibration interactions.

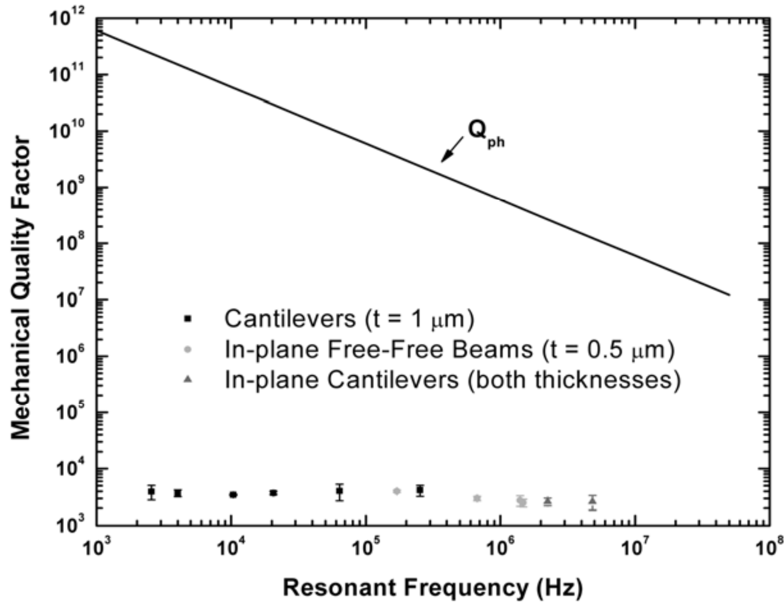

Fig. 5.11. Plot of the quality factor in ta-C oscillators versus resonant frequency. The solid line shows the theoretical maximum value of quality factor if the dissipation was limited by phonon-mechanical vibration interaction in the oscillators.

As can be seen in these plots, the quality factor for ta-C remains constant at about 2 - 4 × 10^3 for nearly all of oscillators measured throughout the frequency span of about 1 × 10^3 Hz to 5 × 10^6 Hz. The insensitivity of Q with frequency is not consistent with internal dissipation in ta-C being limited by intrinsic dissipation mechanisms or dissipation due to a specific defect with a single characteristic relaxation time. In this latter case, Q would be expected to vary as ω^{-1} or ω, depending on the value of the defect relaxation time compared to the oscillator frequency.

For amorphous materials, a form of extrinsic internal dissipation has often been observed which may be best characterized as dissipation due to a spectrum of defects with a broad range of relaxation times. This behavior is most striking when one examines the internal dissipation in these materials at low temperature. In this regime there is a remarkably universal behavior exhibited by materials ranging from silica glasses, a-Si, a-Ge, disordered multi-component oxides, numerous polymers, various selenides, and arsenides [27-29]. In amorphous materials, the internal dissipation was observed to exhibit a temperature independent plateau at a limiting value of 10^3 to 10^4. The accepted explanation for the plateau behavior is that there exists in these materials a "universal" process of phonon-assisted quantum mechanical tunneling of atoms or collections of atoms amongst a broad distribution of tunneling states (TS) [30,31].

Historically, the TS have been described as non-interacting two-level systems. At low temperatures, the system can quantum mechanically tunnel between states, leading to a temperature independent source of dissipation. Additionally, it is assumed that there exists a smooth distribution of energy differences, ΔE, between two-level states and that the concentration of TS is proportional to T. In other words, the density of tunneling states, $n(\Delta E)$, measured in concentration per unit energy, is independent of T, i.e. flat. In the TS regime, it is also expected that the dissipation is independent of oscillator frequency, ω. In practice, a slight frequency dependence has been observed in some amorphous materials [28]. In the high

temperature regime, the distribution of defect states for many amorphous materials is not flat, and both a frequency and temperature dependence may be found [28].

The ta-C material exhibited a frequency independent Q and a magnitude of Q that was characteristic of amorphous materials in the low temperature regime, i.e. behavior that was similar to TS defect controlled, except at a much higher temperature. Given that the measurement temperature is too high for tunneling between defect states to be limiting, we have assumed that a spectrum of defect states, characterized by a spectrum of relaxation times, must exist in ta-C. The activation energies for the relaxation processes that occur in this material may be estimated from Eq. 5.17, using $\tau_0 = 10^{-13}$ sec. The calculated activation energy distribution is shown in Fig. 5.12. Assuming the mechanical relaxation per defect is the same for all defects, then the measured quality factor is a relative measure of defect concentration, and this yields a relatively flat defect distribution over the energy range from about 0.35 to over 0.55 eV.

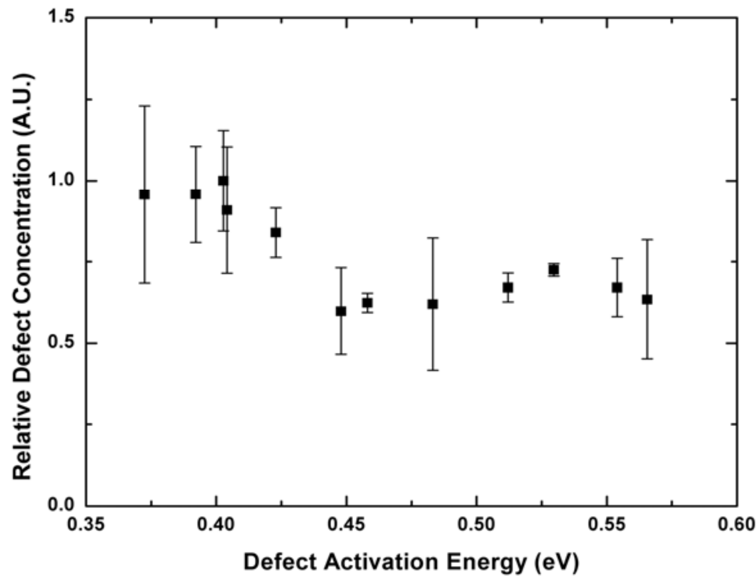

Fig. 5.12. Plot of the relative defect concentration versus activation energy for the proposed defects that limit the value of the quality factor. The variation in relative defect concentrations was less than a factor of 2 for activation energies ranging from approximately 0.35 to 0.55 eV. (The defect concentrations were normalized to the largest value.)

The atomic nature of the defects that control dissipation in ta-C is not known. The measured defect activation energies are lower than either the activation energy for vacancy self-diffusion in crystalline diamond, which is about 2.3 eV [32] or the activation energy for self-interstial diffusion in diamond, which is about 1.3 eV [33]. This suggests that the defect relaxation process in ta-C does not involve atomic diffusion; therefore, localized defect relaxations would be a more probable cause.

In many amorphous materials, relaxation processes are assumed to be associated with hopping of atoms between nearly energetically degenerate structural configurations. For example, a loss peak at approximately 40 K is often observed in bulk amorphous SiO_2, corresponding to an approximate activation energy of 0.05 eV. This loss peak is thought to arise from the thermally activated hopping of a bridging O atom between two nearly degenerate equilibrium positions [34]. Similar processes might be expected in ta-C. In one study of internal

dissipation in amorphous carbon films of varying 4-fold content, the room temperature dissipation was similar to that reported here, but a strong temperature dependence was observed in the range of 10 K to 300 K [35]. The authors attributed the dissipation to structural disorder in the films, but the nature of the defects was not identified. In a similar material, nanocrystalline diamond, Q's comparable to those measured here were found at frequencies ranging from about 6 MHz to 30 MHz, again suggesting that similar defect relaxation processes may be operative [36]. Future experiments will investigate the temperature dependence of Q in ta-C in order to obtain more information about the nature of the atomic relaxation processes.

5.7 Conclusions

We have fabricated oscillators from a tetrahedrally-coordinated amorphous carbon material. We measured the resonant frequencies and calculated the quality factors using oscillators of several different designs and widely varying dimensions. We observed quality factors of approximately $2 - 4 \times 10^3$ for nearly all oscillators with resonant frequencies ranging from the low kHz to several MHz. By inspecting the different dissipation mechanisms that commonly limit the quality factor, we determined that these oscillators were not limited in quality factor by air or squeeze film damping or by clamping losses. Additionally, by using the mechanical and thermal properties of ta-C, we determined that the oscillators were not limited by thermoelastic dissipation or by dissipation due to phonon-mechanical vibration interaction. However, dissipation due to mechanical defects that are inherent to the ta-C structure was found to be consistent with the observed frequency dependence of the quality factor. We found that the mechanical dissipation in this material was well-described by a flat spectrum of defects with activation energies ranging from about 0.35 eV to over 0.55 eV.

Knowledge of the limiting value of the quality factor for the different oscillator designs and dimensions provides an upper boundary for the sensitivity of these oscillators in sensor applications. By fabricating new devices with higher frequencies, we hope to determine the extent and relative concentrations of the dissipative defects seen in ta-C. Also, future studies will examine the temperature dependence of mechanical dissipation in this material in order to determine the full extent of the range of dissipative defects in this material and to shed more light on their origins.

5.8 References

1. K. E. Petersen, Proc. IEEE **70**, 420 (1982).
2. C. T.-C. Nguyen, L. P. B. Katehi, and G. M. Rebeiz, Proc. IEEE **86,** 1756 (1998).
3. J. J. Yao, J. Micromech. Microeng. **10**, R9 (2000).
4. G. T. A. Kovacs, *Micromachined Transducers Sourcebook* (McGraw-Hill Book Company, New York 1998).
5. S. J. Martin, M. A. Butler, J. J. Spates, M. A. Mitchell, and W. K. Schubert, J. Appl. Phys. **83**, 4589 (1998).
6. B. Ilic, D. A. Czaplewski, H. G. Craighead, P. Neuzil, C. Campagnolo, and C. Batt, Appl. Phys. Lett. **77**, 450 (2000).
7. B. Ilic, D. A. Czaplewski, H. G. Craighead, P. Neuzil, C. Campagnolo, and C. Batt, J. Vac. Sci. Technol. **B19**, 2825 (2001).
8. J. P. Sullivan, T. A. Friedmann, and K. Hjort, MRS Bull. **26**, 309 (2001).

9. B. E. N. Keeler, D. W. Carr, J. P. Sullivan, T. A. Friedmann, and J. R. Wendt, Optics Lett. **29**, 1182 (2004).
10. T. M. Alam, T. A. Friedmann, P. A. Schultz, and D. Sebastiani, Phys. Rev. B **67**, 245309 (2003).
11. H. Hosaka, K. Itao, and S. Kuroda, Sens. Actuators A **49**, 87 (1995).
12. F. R. Blom, S. Bouwstra, M. Elwenspoek, and J. H. J. Fluitman, J. Vac. Sci. Technol. B **10**, 19 (1992).
13. V. B. Braginsky, V. P. Mitrofanov, V. I. Panov, Systems with Small Dissipation (University of Chicago Press, Chicago, 1985).
14. L. D. Landua and E. M. Lifshitz, *Theory of Elasticity* (Pergamon Press, New York, 1970).
15. T. V. Roszhart, in *Tech. Dig. Solid-State Sens. Actuator Workshop*, Hilton Head, SC 1990, pp. 13-16.
16. R. Lifshitz and M. L. Roukes, Phys. Rev. B **61**, 5600 (2000).
17. K. Y. Yasumura, T. D. Stowe, E. M. Chow, T. Pfafman, T. W. Kenny, B. C. Stipe, and D. Rugar, J. Microelectromech. Syst. **9**, 117 (2000).
18. J. Yang, T. Ono, and M. Esashi, J. Microelectromech. Syst. **11**, 775 (2002).
19. J. F. Berret and M. Meissner, Z. Phys. B **70**, 65 (1988).
20. A. S. Nowick and B. S. Berry, *Anelastic Relaxation in Crystalline Solids* (Academic Press, New York, 1972).
21. D. W. Carr, S. Evoy, L. Sekaric, H. G. Craighead, and J. M. Parpia, Appl. Phys. Lett. **75**, 920 (1999).
22. J. A. Henry, Y. Wang, and M. A. Hines, Appl. Phys. Lett. **84**, 1765 (2004).
23. S. Timoshenko, D. H. Young, and W. Weaver Jr., *Vibrational Problems in Engineering* (John Wiley & Sons, Inc., New York, Chapter 5, 1974).
24. W.-T. Hsu, J. R. Clark, and C. T.-C. Nguyen, Digest of Technical Papers, the 11th Int. Conf. on Solid-State Sensors & Actuators (Transducers '01), Munich, Germany, 2001, pp. 1110.
25. J. M. Bustillo, R. T. Howe, and R. S. Muller, Proc. IEEE **86**, 1552 (1998).
26. D. W. Carr, J. P. Sullivan, T. A. Friedmann, Optics Lett. **28**, 1636 (2003).
27. J. Y. Duquesne and G. Bellessa, Phil. Mag. B **52**, 821 (1985).
28. K. A. Topp and D. G. Cahill, Z. Phys. B **101**, 235 (1996).
29. X. Liu, B. E. White, Jr., R. O. Pohl, E. Iwanizcko, K. M. Jones, A. H. Mahan, B. N. Nelson, R. S. Crandall, and S. Veprek, Phys. Rev. Lett. **78**, 4418 (1997).
30. P. W. Anderson, B. I. Halperin, and C. M. Varma, Philos. Mag. **25**, 1 (1972)
31. W. A. Phillips, J. Low Temp. Phys. **7**, 351 (1972).
32. G. Davies, S. C. Lawson, A. T. Collins, A. Mainwood, S. J. Sharp, Phys. Rev. B **46**, 13157 (1992).
33. J. F. Prins, Phys. Rev. B **44**, 2470 (1991).
34. O. Anderson and H. Bömmel, J. Amer. Ceram. Soc. **38**, 125 (1955).
35. X. Liu, D. M. Photiadis, J. A. Bucaro, J. F. Vignola, B. H. Houston, H.-D. Wu, and D. B. Chrisey, Mat. Sci. Eng. A **370**, 142 (2004).
36. L. Sekaric, J. M. Parpia, H. G. Craighead, T. Feygelson, B. H. Houston, and J. E. Butler, Appl. Phys. Lett. **81**, 4455 (2002).

6.0 NEMOs Optomechanical Structures

6.1 Introduction

Microelectromechanical systems (MEMS) technology has developed rapidly over the past few decades. One of the most important commercial applications for MEMS has been the field of inertial sensors, and accelerometers in particular. There is a large demand for high-sensitivity accelerometers in such areas as navigation and guidance systems, microgravity measurements, and earthquake prediction. The broad use of MEMS inertial sensors is in great part due to their low cost and inherently small size and weight.

6.2 Experiment and Results

In this section we consider a laterally deformable optical NEMS (nanoelectromechanical systems) grating transducer, schematically illustrated in Fig. 6.1. Deformable optical gratings have previously been studied for applications in displays, sensors, and optical switches for communications [1,2]. Here, however, we discuss the use of such a device as a micromachined accelerometer. For small changes in the spacing of the nanostructured grating elements, a large change in the optical reflection amplitude is observed. This anomalous diffraction property was predicted in a previous work [3]; here, we experimentally verify operation of these devices and demonstrate a motion detection sensitivity comparable to or exceeding that of any other MEMS transducer. As optical devices, these sensors have additional advantages over other electrical sensors, including high immunity to electromagnetic interference and the possibility of integration with fiber optics to create a network of sensors with a single remote optical source and detector.

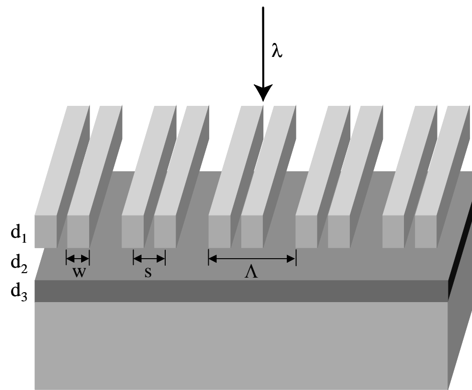

Fig. 6.1. Cross section of the laterally deformable grating. The thicknesses of the grating, air gap, and antireflection coating regions are d_1, d_2, and d_3, respectively. The width of an individual grating element is w, and the center-to-center nearest neighbor spacing is s. The grating period is Λ. Light is incident normal to the plane of the grating.

The devices were fabricated in tetrahedral amorphous carbon, also known as amorphous diamond (aD), using a surface micromachining process similar to that used for the fabrication of polysilicon MEMS [4,5]. An amorphous diamond film with a thickness of 0.4 μm was deposited onto a substrate consisting of 2 μm of SiO_2 on 0.2 μm of Si_3N_4 on silicon. Additionally, a layer

of polysilicon, about 0.1 μm thick, was used between the amorphous diamond and SiO_2 to improve interface adhesion.

The devices were made by first photolithographically patterning 320 μm x 720 μm pads of aluminum on the aD surface. Electron beam patterning was then used to define arrays of gratings aligned to the aluminum contact pads, followed by lift-off of the aluminum layer. The aD layer was etched with the aluminum layer acting as a mask. Following dry etching, the contact pads connected to the grating devices were metallized with a combination of titanium and gold. Next, wet etching of the SiO_2 sacrificial layer was performed. Following wet etching, the structures were dried in flowing N_2 gas, and a brief dehydration bake was used to free the aD structures from the substrate.

The width of the individual grating beams (nominally 50 or 100 nm) and the nearest-neighbor spacing (180 or 230 nm) differ from device to device, while the grating pitch is fixed at 600 nm (corresponding to operation at a wavelength of 630 nm). The beam length varies between 1.6 and 6.4 μm, and the total device size ranges from 2 x 6 μm to 8 x 6 μm. An example device is shown in Fig. 6.2.

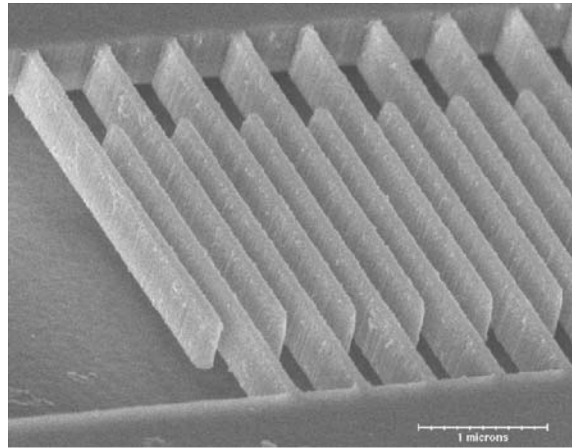

Fig. 6.2. SEM micrograph of a typical grating structure measured in this work. The beam width, w, of this grating is 50 nm and the vertical thickness, d_1, is 400 nm. The period, Λ, of the two-element grating is 600 nm, and the nearest neighbor spacing, s, is 180 nm. The length of each beam is 3.2 μm.

The finished devices were fixed in a 24-pin package, and wire bond connections were made to provide electrical contact. Neighboring beams are deflected toward one another by applying a voltage across them, thereby changing the relative spacing of grating elements within the grating period. The device sample was mounted in a small vacuum chamber to allow reduction to pressures below 1 mTorr. TE-polarized light from a tunable HeNe laser was focused onto the device to a spot size of approximately 2 μm using a long-working-distance microscope objective. The reflected light was captured by a 1-GHz bandwidth silicon photodetector, and the resulting signal was input to a tracking RF spectrum analyzer. The devices were driven by the RF output of the same spectrum analyzer. A dc bias was added to the signal, such that the total voltage on the device was of the form $V = V_{dc} + V_{ac} \sin(\omega t)$.

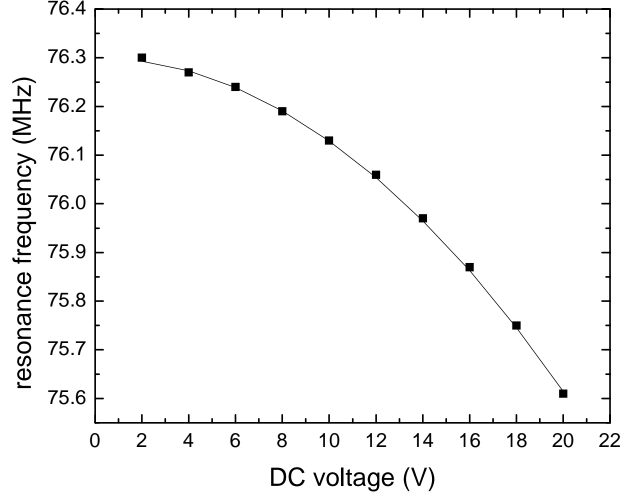

Fig. 6.3. A plot of the resonance frequency shift as a function of applied dc voltage for one device. The squares are measured data, and the curve is the theoretical fit using an electrostatic model.

The resonance response of the devices was determined by sweeping the drive frequency while applying a dc voltage and measuring the amplitude of the reflected optical signal at the driving frequency. From this data the quality factor of the device could be determined, using:

$$Q = \frac{f_0}{\Delta f_{3dB}} \tag{6.1}$$

For devices of various lengths and widths, the measured resonance frequencies ranged from 6 to 80 MHz, and the quality factor from 100 to 200. The shift of the resonant frequency with applied dc voltage was also measured (Fig. 6.3). This behavior can be modeled by approximating each pair of beams as an isolated parallel plate capacitor. Assuming small deflections of the beam and small ac voltage, the resonance frequency depends on the bias voltage as:

$$\omega_r = \sqrt{\omega_0 - \frac{\varepsilon_0 A}{m_{eff} d_0^{\ 3}} V_{dc}^{\ 2}}, \tag{6.2}$$

where A is the cross-sectional area of one beam, m_{eff} is the effective modal mass [6], and d_0 is the initial separation between the beams. The natural resonance frequency, ω_0, of each device follows the relation:

$$\omega_0 = \sqrt{\frac{Ew^2}{12\rho}}\left(\frac{1.875}{L}\right)^2 \tag{6.3}$$

where E=670 GPa is the Young's modulus for aD, ρ=2900 kg/m^3 is the density of aD, and L is the length of the beams. By applying equation 6.2 to the data, the physical parameters of the device were extracted. The data shows a good fit to this approximation.

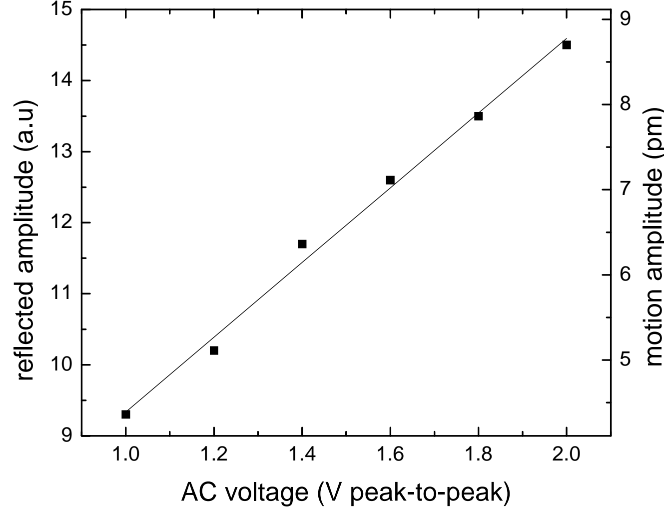

Fig. 6.4. Reflected optical amplitude at 100 Hz as a function of applied ac voltage, for the same device measured in Fig. 6.3. The squares are the measured data. The solid line, corresponding to the right-hand axis, is indicative of the equivalent amplitude of motion based on electrostatic calculations.

The low-frequency response of the devices was also measured by replacing the 1 GHz detector with an autobalanced photoreceiver. The reflected optical amplitude was measured as a function of the RF drive voltage at 100 Hz (off resonance), while the dc voltage was held constant at a small value. The results are plotted in Fig. 6.4, where the solid line represents the corresponding calculated amplitude of the mechanical deflection. Again using the electrostatic model and assuming small deflections, the dependence of the deflection, *x*, on the voltage is:

$$x = \frac{\varepsilon_0 A}{2 m_{eff} \omega_0^2 d_0^2} V^2 . \qquad (6.4)$$

Because a small ac voltage is added to the dc voltage, a cross term at the driving frequency results, which is linearly dependent on the two voltages:

$$x_\omega = \frac{\varepsilon_0 A}{m_{eff} \omega_0^2 d_0^2} V_{dc} V_{ac} \sin(\omega t) . \qquad (6.5)$$

Since the reflection amplitude is also linear in the ac driving voltage, it follows that the reflection amplitude is linear with the mechanical deflection (for components at the driving frequency). From the data, the detection sensitivity can be determined. When measured with a 1 Hz bandwidth, the standard deviation of the data for this device corresponds to a minimum resolvable motion of 160 fm.

These preliminary results demonstrate a clear potential use for these devices in sensor applications, although we still expect to see substantial improvements to the displacement sensitivity. For example, the data shown in Fig. 6.4 are from a device that is only 2 x 6 μm in

size. Expanding the size would allow more of the light to be incident on the active area. Furthermore, a larger device would enable the use of a collimated beam, rather than the 0.35 NA converging beam used here. Simulations indicate that when the waves are incident from off-axis, a reduced amount of reflectance modulation will be seen for a given range of movement. Because the experiments reported here used a converging beam, it is difficult to precisely correlate this data with the simulation predictions. Additionally, the current devices lack an anti-reflective layer, which would be present in an ideal structure. Mitigating all of these effects through design improvements should enhance the sensitivity by 1.5 to 2 orders of magnitude.

We are currently fabricating grating structures with somewhat larger sized features, with the intention of addressing some of the above problems. Structures with 0.25 μm critical features can be patterned using conventional photolithography techniques, yet still display a similar level of motion sensitivity. This same effect can also be seen as the wavelength is increased, as long as the device dimensions are scaled appropriately. Using this type of structure with 1.55 μm light, for instance, should be quite possible, and could even lead to applications suitable for optical communications.

The use of the laterally deformable grating structure as a motion transducer offers additional advantages over other sensors with similar levels of sensitivity, such as electron tunneling or Fabry-Perot transducers. The in-plane motion of this grating structure is highly desirable, as it enables the design of devices with multiple degrees of freedom on the same chip. Using polarization diversity, it may be possible to create a 3-axis sensor employing a single transducer. The linear range of motion of this device (10 - 100 nm) can also be very large in comparison to that of tunneling transducers (0.01 nm), which will relax some of the requirements on the feedback control used in the sensing system.

6.3 Conclusion

We have experimentally verified the operation of a laterally deformable optical grating transducer. This class of device has a broad range of applications, including as an optical modulator for communications or display technologies, as a polarizing beamsplitter, and in accelerometers and other inertial sensing systems. The nanomechanical devices were fabricated in amorphous diamond using standard lithographic techniques. A detection limit of 160 fm/ Hz was measured, approaching that of the best tunneling transducers and exceeding that of any other micromechanical transducers [7]. Increasing the device area and illuminating it with plane waves, rather than a focused beam, could further increase the sensitivity of this device by up to two orders of magnitude. In future work, these devices will be incorporated into a complete system.

6.4 References

1. R. B. Apte, F. S. A. Sandejas, W. C. Banyai, and D. M. Bloom, Tech. Dig. Solid-State Sensor and Actuator Workshop **1** (1994).
2. O. Solgaard, F. S. A. Sandejas, and D. M. Bloom, Opt. Lett. **17**, 688 (1992).
3. D. W. Carr, J. P. Sullivan, and T. A. Friedmann, Opt. Lett. **28**, 1636 (2003).
4. J. P. Sullivan, T. A. Friedmann, M. P. de Boer, D. A. LaVan, R. J. Hohlfelder, C. I. H. Ashby, M. T. Dugger, M. Mitchell, R. G. Dunn, and A. J. Magerkurth, Proc. Materials Research Society Symposium **657**, EE711 (2001).

5. J. P. Sullivan, T. A. Friedmann, and K. Hjort, MRS Bull. **26**, 309 (2001).
6. A. A. Shabana, *Vibration of Discrete and Continuous Systems* (Springer, 1997).
7. C. H. Liu and T. W. Kenny, J. Microelectromech. Systems **10**, 425 (2001).

7.0 RF MEMS Switches with ta-C Dielectrics

7.1 Introduction

Radio frequency microelectromechanical systems (RF MEMS) capacitive switches exhibit several advantages over solid state switches, including better isolation, reduced insertion loss, and lower static power dissipation [1]. However, a key factor limiting the lifetime of these switches is charge injection and retention, due to the high electric field created in the switch dielectric by the actuation voltage [2,3]. Charge build-up interferes with the operation of the device, manifesting itself as incremental changes in the actuation voltage, failure of the device to release once the actuation voltage is removed, or unintentional release of the device while the actuation voltage is applied [3]. The identification of the mechanisms of charging and the development of methods for its control are crucial, if these technologies are to become practicable. Recently, the use of dielectric materials with 'tunable' resistivity has been proposed as a potential method for mitigating fixed charge induced failure of electrostatically-actuated MEMS devices [4]. By providing a relatively low impedance path for trapped charge to leave the dielectric, actuation voltage drift and adhesion could be potentially controlled. Tetrahedral amorphous carbon/amorphous diamond (aD) is an unconventional dielectric with electrical conductivity governed by tunnelling or hopping conduction between clusters of π-bonded carbon [5]. The concentration of π-bonded clusters can be varied to control the resistivity over 8 orders of magnitude (from about 0.1 to 10^7 Ωcm) enabling tuning of the dielectric conductance and dissipation characteristics. The surface is hydrophobic, reducing adhesion during operation due to capillary forces (i.e. stiction), and potentially allowing for the development of more compliant switch membranes for lower voltage actuation. Currently, very little is known about the charge retention behavior of this material and its applicability to MEMS switches. In this section, we attempt to validate its use in these devices.

7.2 Fabrication

The switch test structures, shown in Fig. 7.1, are fabricated in a three-level, surface micromachining process. The switch dielectric is 4000 Å -thick, pulsed laser deposited aD (a room temperature process [5]) and is patterned simultaneously with a 2000 Å -thick tungsten film underneath, which acts as the bottom electrode. A sacrificial polymer layer is spun on and patterned over these films. The top mechanical layer is approximately 2 μm of electroplated Au, which comprises both the ground traces and the combined signal/bridge trace of the CPW structure. The devices are released in an O_2/CF_4 plasma at 100ºC. The switch is actuated by an electrostatic attraction force between the grounded bottom shunt metal and the suspended signal bridge, which is biased with a DC voltage of 10 to 30 V. When actuated, the large capacitance of the bridge/shunt contact area represents a low impedance path to ground for RF energy, effectively turning 'off ' the switch.

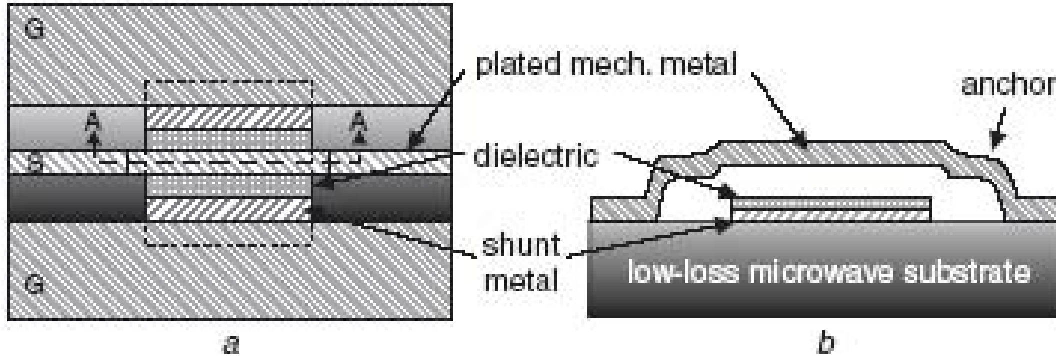

Fig. 7.1. RF MEMS switch. (a) Top view. (b) Side view.

7.3 Results and Discussion

S-parameter measurements of the switch RF performance were taken using an HP 8510C network analyzer with an in-line DC bias capability. The measured isolation for this test structure in the down-state exceeds 18 dB at 18 GHz, as shown in Fig. 7.2. This result may be modeled as a down-state capacitance of approximately 2.6 pF, demonstrating a high shunt capacitance. This value is smaller than expected and most likely due to a non-ideal contact area and significant roughness of the bridge and dielectric surfaces.

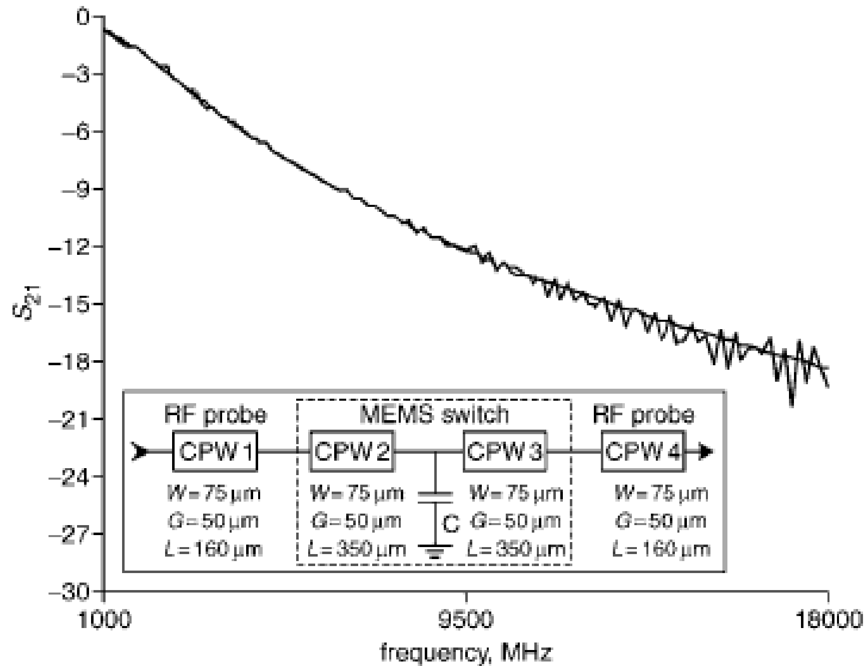

Fig. 7.2. Measured and modeled RF isolation of aD capacitive switch.

The aD films used in these test devices exhibited a resistivity of about 6×10^9 Ωcm and a breakdown strength of about 1 MV/cm, as measured on an Agilent 4156C parameter analyser. Based on these data, for an actuation voltage of 10 V and a film thickness of 4000 Å , we predict a down-state static power dissipation of 10 nW. This compares favorably with existing switching

technologies (e.g. PIN diode), which typically consume milliwatts of power in static operation. This result also demonstrates one of the key benefits of applying aD films to capacitive switch designs – the ability to selectively deposit controlled resistivity films. With this capability, the optimal balance can be made between the charge leakage behavior desired for proper switch functionality and the static power dissipation required for practical use in low-power applications. The initial switching performance of the test switch was measured using a unipolar triangle wave, which allows the extraction of both the actuation and release voltage values from the switch response. Typical charging dielectrics (e.g. SiN) used in electrostatic devices exhibit a 'bipolar' response to a unipolar stimulus over time, due to a parasitic electric field created between the electrodes by the trapped charge. The field due to the trapped charge, ρ_s, will induce a shift in the relative bias potential of the bottom electrode, with respect to the bridge:

$$V_{os} = \frac{z\rho_s}{\varepsilon_d}. \tag{7.1}$$

With successive cycles of the stimulus signal, the offset potential will continue to shift as more charge accumulates in trap sites in the dielectric. If the peak-to-peak magnitude of the unipolar stimulus signal is sufficiently high, then it will be possible to induce actuation at two bias points per stimulus cycle, analogous to the response to a bipolar stimulus with twice the frequency. The induced movement of charge in response to the applied stimulus eventually reaches an equilibrium condition where the relative mobilities and trapping densities for the two charge carriers balance. An example of this behavior is shown in Fig. 7.3, for a switch using a silicon oxynitride (SiON) dielectric. Therefore, unless the charge trapping behavior of a particular dielectric is known precisely, it will be very difficult to predict the magnitude of this actuation voltage drift in a typical capacitive switch design. For our test structures, the response of the test switch to a unipolar 9 V triangle wave is shown in Fig. 7.4 and is unipolar, consistent with a non-charging dielectric. The measured actuation voltage for switch closure is approximately 8 V and for release is 3 V. Goldsmith et al. showed that for a small actuation bias (< 40 V), the amount of dielectric charging is reduced and the lifetimes of capacitive switches are exponentially higher [2]. We are currently investigating the response of our test structures to increased bias magnitudes in order to more thoroughly establish the charging behavior of aD under higher voltage stresses.

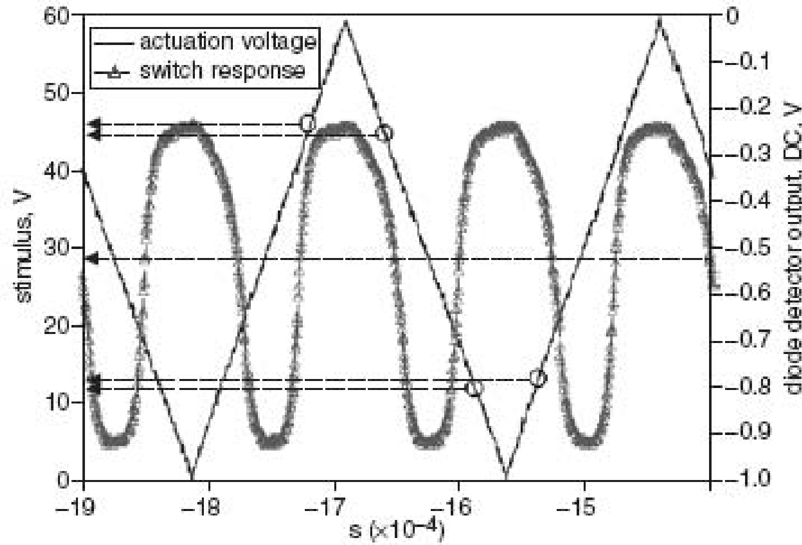

Fig. 7.3. Unipolar actuation and bipolar response of SiON capacitive switch.

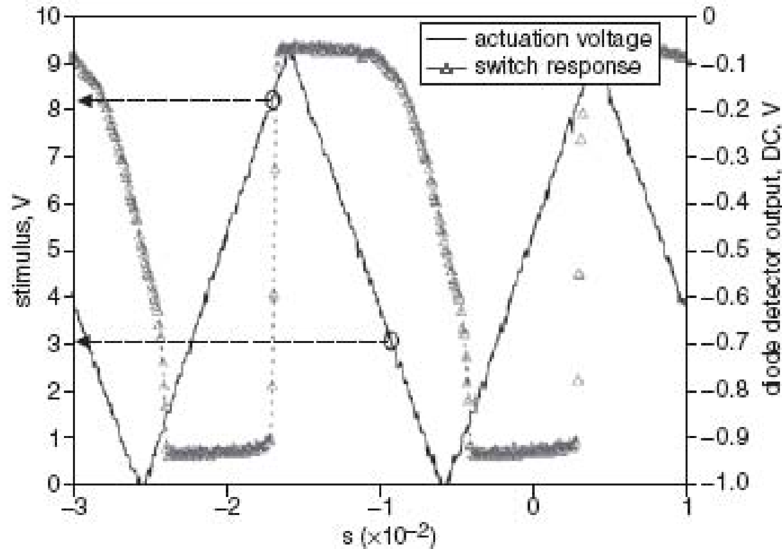

Fig. 7.4. Unipolar actuation and bipolar response of aD capacitive switch.

7.4 Conclusion

We have successfully demonstrated the incorporation of amorphous diamond into RF MEMS capacitive switches. Fabricated devices exhibited a down-state response consistent with a capacitance of 2.6 pF, an expected static power dissipation of 10 nW and noncharging behaviour based on their response to a unipolar stimulus. These results support the use of aD materials to improve the reliability and performance of RF MEMS capacitive switches.

7.5 References

1. G. M. Rebeiz and J. B. Muldavin, IEEE Microw. Mag. **2**, 59 (2001).
2. C. Goldsmith, et al., IEEE MTT-S Int. Microw. Symp. Dig. **1**, 227 (2001).

3. J. R. Reid and R. T. Webster, Electron. Lett. **38**, 1544 (2002).
4. N. Hoivik, et al., IEEE MTT-S Int. Microw. Symp. Dig. **2**, 1229 (2002).
5. J. P. Sullivan, T. A. Friedmann, and K. J. Hjort, MRS Bull. **26**, 309 (2001).

8.0 Future

Many challenges remain for successfully integrating NEMOs into electrical circuits as filters for RF electrical signals. Certainly, small mechanical oscillators with very high resonant frequencies can be created and measured. Our smallest NEMOs exhibit fundamental resonant frequencies that exceed 100 MHz, and there have been reports in the literature of other nano-scale oscillators with purported resonant frequencies exceeding 1 GHz [1]. The target frequencies for RF electrical circuits keep increasing, however, ranging from about 2.4 GHz for cellular communications to ~ 17 GHz or more for radar. These frequencies lie above the region accessible with reasonable-sized (10's of nm) nano-scale transverse-mode mechanical oscillators. Indeed, the more feasible technological approach for mechanical filtering involves the use of film bulk acoustic resonators [2]. These mechanical resonators are macro-scale (millimeter-sized) devices that operate on the principle of exciting a shear mode of a piezoelectric thin film material. Since they involve actuation of a "stiff" mode of a macroscopic structure, high resonant frequencies are achievable. These stiff modes, however, require higher forces to excite, which translates into higher power requirements for the electrical signal. Therefore, these structures are not suitable for extremely small signal levels or for the detection of extremely small forces, which is the true advantage of nanomechanical oscillators.

With the realization that nanomechanical oscillators are most advantageous for their extreme sensitivity to small forces, it is clear that the optimum field of use is in the area of sensing. This is one of the motivations for their use in the optomechanical device described in section 6 of this report. Numerous other sensor approaches may be envisioned, including simple cantilever array-based chemical sensors using structures similar to those shown in Fig. 1.1., for example. The successful development of sensors for extremely small forces relies on the control of the quality factor, Q, of the oscillator. For example, the minimum detectable force that can be achieved with a small mechanical oscillator scales as $Q^{-1/2}$ [3], which necessitates the development of high Q oscillators.

Understanding what limits Q in small mechanical oscillators is a very difficult, yet very important field of research. This forms the basis for some of the key scientific questions regarding the mechanics of nano-scale structures. In contrast, other aspects regarding the mechanics of small structures are on a much firmer footing. For example, studies have shown that continuum elasticity theory works adequately for mechanical structures down to the 10's of nm length scale (the common minimum size for practical mechanical structures). Significant deviations are only seen when dimensions approach the few nm length scale, in which case the mechanical properties of atoms near the free surfaces become important [4]. Therefore, in most cases the bulk mechanical behavior of small structures may be predicted rather accurately. This is, unfortunately, not the case for predicting how energy is dissipated in these structures.

Several key scientific questions can be posed regarding dissipation in small structures: (1) what limits Q in small mechanical structures, (2) why do the Q's decrease with decreasing oscillator size, even for single crystal oscillators, (3) why do most small oscillators exhibit the same Q at low temperatures, independent of oscillator material (being about 10^3 to 10^5), and (4) what is the mechanism that causes this size-limited Q to correspond to the Q that is measured for nearly all amorphous materials? The gap in our understanding can be illustrated by reference to recent experiments and theory of internal dissipation in small mechanical oscillators. For example, Mohanty et al. have discovered in their experiments that small single crystal Si and GaAs mechanical oscillators exhibit a near saturation in Q as the temperature is decreased below

about 80 K [5]. This behavior is not observed in larger mechanical oscillators. Based on the similarity in Q saturation in these small systems to that observed in amorphous materials, Ahn and Mohanty have described the dissipation as being due to tunneling states dissipation (a form of dissipation thought to be operative in amorphous materials) [6]. This is a quantum mechanical tunneling form of dissipation that would not be expected classically. Recently, however, Jiang et al. [7] performed a classical molecular dynamics study of dissipation in a small section of carbon nanotube and observed a very similar saturation in the Q to that observed experimentally by Mohanty et al. Clearly, the classical simulation cannot include quantum mechanical tunneling, suggesting that the dissipation in small systems must have some other, as yet unknown, cause. One possibility that we suggest is that the dissipation in small systems displays an unexpected temperature dependence because one key form of classical dissipation, thermoelastic dissipation, becomes strongly temperature dependent due to a transition from diffusive phonon transport to ballistic phonon transport. To our knowledge, this hypothesis has yet to be tested.

What can be said regarding the critical research needs in improving reliability in RF MEMS switches? Here the problem is one of materials development – specifically, the need to develop a thin film material that is compatible with MEMS and that has very specific mechanical, electronic, and chemical properties. In the case of capacitively-coupled switches, the key requirements are that the dielectric needs to be charge-dissipating, smooth, mechanically hard, and stiction resistant. The ta-C material is attractive for all of these properties. However, the dielectric breakdown field strength is less than that which is desired (being about 1 – 2 MV/cm, instead of the 3 – 4 MV/cm or more that would be preferred). The dielectric breakdown field strength in this material may potentially be increased by the addition of Si, as has been demonstrated for thin film diamond-like carbon based dielectrics used in capacitors. In the case of contact RF MEMS switches, an entirely different set of material properties are required, namely the need for a high conductivity contact metal that is mechanically hard and resistant to contact wear and contact welding during hot switching. The search for suitable thin film metallic contacts is a current active area of research.

8. 1 References

1. X. M. H. Huang, C. A. Zorman, M. Mehregany, and M. L. Roukes, Nature **421**, 496 (2003).
2. S.-H. Park, B.-C. Seo, H.-D. Park, and G. Yoon, Jpn. J. Appl. Phys. **39**, 4115 (2000).
3. V. B. Braginsky, V. P. Mitrofanov, and V. I. Panov, *Systems with Small Dissipation* (University of Chicago Press, Chicago, 1985).
4. D. E. Segall, S. Ismail-Beigi, and T. A. Arias, Phys. Rev. B **65**, 214109 (2002).
5. P. Mohanty, D. A. Harrington, K. L. Ekinci, Y. T. Yang, M. J. Murphy, and M. L. Roukes, Phys. Rev. B **66**, 085416 (2002).
6. K.-H. Ahn and P. Mohanty, Phys. Rev. Lett. **90**, 085504 (2003).
7. J. Jiang, M.-F. Yu, B. Liu, and Y. Huang, Phys. Rev. Lett. **93**, 185501 (2004).

9.0 Acknowledgments

The authors gratefully acknowledge R. Doty and B. Mckenzie for experimental assistance and N. Modine and S. Hearne for valuable discussions and comments. This work was supported by a Laboratory Directed Research and Development project at Sandia National Labs, Albuquerque, NM.

DISTRIBUTION

5	MS 1421	J. P. Sullivan, 1112
1	MS 1415	D. E. Peebles, 1112
1	MS 1415	J. C. Barbour, 1110
1	MS 1427	J. M. Phillips, 1100
1	MS 1415	T. A. Friedmann, 1112
1	MS 1415	D. A. Czaplewski, 1112
1	MS 0603	C. W. Dyck, 1742
1	MS 0603	J. R. Webster, 1742
1	MS 0603	A. J. Carton, 1742
1	MS 1080	D. W. Carr, 1769
1	MS 1080	B. E. N. Keeler, 1769
1	MS 0603	J. R. Wendt, 1743
1	MS 1411	D. R. Tallant, 1822
1	MS 0889	B. L. Boyce, 1851
1	MS 0918	Central Technical Files, 8945-1
2	MS 0899	Technical Library, 9616
2	MS 0123	D. L. Chavez, LDRD Office, 1011